LA-UR-22-22963
Accepted Manuscript

FORTE Measurements of Global Lightning Altitudes

Peterson, Michael Jay

Provided by the author(s) and the Los Alamos National Laboratory (2022-10-11).

To be published in: Earth and Space Science

DOI to publisher's version: 10.1029/2022EA002404

Permalink to record:
http://permalink.lanl.gov/object/view?what=info:lanl-repo/lareport/LA-UR-22-22963

Los Alamos National Laboratory, an affirmative action/equal opportunity employer, is operated by Triad National Security, LLC for the National Nuclear Security Administration of U.S. Department of Energy under contract 89233218CNA000001. By approving this article, the publisher recognizes that the U.S. Government retains nonexclusive, royalty-free license to publish or reproduce the published form of this contribution, or to allow others to do so, for U.S. Government purposes. Los Alamos National Laboratory requests that the publisher identify this article as work performed under the auspices of the U.S. Department of Energy. Los Alamos National Laboratory strongly supports academic freedom and a researcher's right to publish; as an institution, however, the Laboratory does not endorse the viewpoint of a publication or guarantee its technical correctness.

Check for updates

23335084, 2022, 9, Downloaded from https://agupubs.onlinelibrary.wiley.com/doi/10.1029/2022EA002404 by Los Alamos National Laboratory, Wiley Online Library on [11/10/2022]. See the Terms and Conditions (https://onlinelibrary.wiley.com/terms-and-conditions) on Wiley Online Library for rules of use; OA articles are governed by the applicable Creative Commons License

AGU ADVANCING EARTH AND SPACE SCIENCE

Earth and Space Science

RESEARCH ARTICLE
10.1029/2022EA002404

FORTE Measurements of Global Lightning Altitudes

Michael Peterson[1]

[1]Los Alamos National Laboratory, ISR-2, Los Alamos, NM, USA

Key Points:

- A new robust data set of very high frequency (VHF) source altitudes from lightning is presented that covers the global Fast On-orbit Recording of Transient Events (FORTE) satellite domain
- Source altitude profiles depend on location, land or ocean terrain, season, and time in the parent flash
- Charge structures can be inferred from FORTE VHF measurements, but accuracy is limited by short view times

Supporting Information:

Supporting Information may be found in the online version of this article.

Correspondence to:

M. Peterson,
mpeterson@lanl.gov

Citation:

Peterson, M. (2022). FORTE measurements of global lightning altitudes. *Earth and Space Science*, *9*, e2022EA002404. https://doi.org/10.1029/2022EA002404

Received 30 APR 2022
Accepted 22 AUG 2022

Author Contributions:

Investigation: Michael Peterson

© 2022 The Authors. Earth and Space Science published by Wiley Periodicals LLC on behalf of American Geophysical Union.
This is an open access article under the terms of the Creative Commons Attribution-NonCommercial-NoDerivs License, which permits use and distribution in any medium, provided the original work is properly cited, the use is non-commercial and no modifications or adaptations are made.

Abstract While multiple lightning detection systems provide geographical locations of lightning events across the globe, robust lightning altitude measurements on a global scale have proven elusive. Space-based platforms have an advantageous viewing geometry for making these measurements, but prior studies with the Fast On-orbit Recording of Transient Events (FORTE) satellite were limited to a few thousand events. In this study, we apply the same technique for calculating source altitude from the previous efforts to a large catalog of hundreds of thousands of global FORTE in-cloud lightning events that were coincident with flashes geolocated by its lightning imager between 1997 and 2003. We use this new data set to document global variations in lightning altitude. As in previous studies, we find that FORTE primarily resolves sources from the upper (positive) charge layer at ~11 km altitude in normal thunderstorms. However, sources are also recorded from other charge layers in the storm and from leaders developing between layers. In particular, we note a pronounced increase in source altitude in the first 20 ms of FORTE flashes from the negative leader developing upward into the upper positive charge layer. Regions known for wintertime and/or stratiform lightning have increased contributions from low-altitude sources, while tropical regions particularly around Panama and the Maritime Continent have the greatest concentrations of high-altitude sources.

Plain Language Summary After many years of observing lightning from multiple sensors, we have a good understanding of how the global frequency of lightning varies from region to region. However, the lightning that we witness on the ground (which is also the primary phenomenon detected by the global lightning detection networks) is only a small portion of the expansive lightning channels. Most of the flash extends through the clouds, hidden from view. The altitudes of lightning flashes in the clouds are particularly important because they reveal changes to convection and play a key role in atmospheric chemistry. In this study, we use a large catalog of in-cloud lightning events recorded by the Fast On-orbit Recording of Transient Events satellite to document variations in lightning altitudes across the globe.

1. Introduction

The altitude of lightning within the cloud is controlled by the kinematics of the parent thunderstorm that organize charged hydrometeors into spatially separated pockets with a surplus of either positive or negative charge. Under typical conditions in the Non-Inductive Charging mechanism (Jayaratne et al., 1983; Mansell et al., 2005; Reynolds et al., 1957; Saunders & Peck, 1998; Saunders et al., 1991; Takahashi, 1978; Takahashi & Miyawaki, 2002), collisions between graupel rimed with supercooled liquid water and small ice particles in the thunderstorm updraft result in the heavier graupel attaining a negative charge and the lighter ice particles becoming positively charged. The updraft sorts these species of hydrometeors by mass, lofting the positively charged ice particles toward the top of the cloud while leaving the negatively charged graupel in the midlevels of the storm. This creates the main positive dipole (Wilson, 1920) that we see in the tripole structure of ordinary thunderstorms (Simpson & Scrase, 1937; summarized in Williams, 1989) that have positive charge regions centered at altitudes of roughly 2 and 10 km and a negative charge layer at 5 km.

However, the diversity and complexity of thunderstorms leads to many different charge structures being observed in nature that diverge substantially from this idealized tripole view. Some storms conflict with the tripole model entirely (i.e., Marshall & Rust, 1991), while others consist of a convective core with a primarily tripole structure adjacent to nonconvective electrified clouds with their own unique charge structures. One notable example of a nonconvective cloud with a distinct charge structure is the electrified anvil cloud. The upper positive layer extends laterally beyond the edge of the convective core into the overhanging anvil, and negative screening layers form on the upper and lower boundaries of the anvil cloud (Marshall et al., 1989). Additionally, electrified stratiform clouds are comprised of multiple vertically confined yet horizontally extensive layers of alternating positive and negative charge created by in situ electrification processes and the advection of charge from the convective

23335084, 2022, 9, Downloaded from https://agupubs.onlinelibrary.wiley.com/doi/10.1029/2022EA002404 by Los Alamos National Laboratory, Wiley Online Library on [11/10/2022]. See the Terms and Conditions (https://onlinelibrary.wiley.com/terms-and-conditions) on Wiley Online Library for rules of use; OA articles are governed by the applicable Creative Commons License

core (Ely et al., 2008; Lang & Rutledge, 2008; Schuur & Rutledge, 2000; Stolzeburg et al., 1998), and stratiform flashes often propagate horizontally at around 6 km altitude (Lang et al., 2004). Thunderstorm charge structures also vary by season and location on Earth (summarized in Williams, 2018), with the inner tropics having particularly tall thunderstorms (López et al., 2019) and winter thunderstorms over the oceans surrounding Japan being well-known for their compact vertical extent (Yamamoto et al., 2006).

Because lightning flashes consist of positive and negative leaders that develop through the thunderstorm charge regions, it is possible to infer the charge structure of a given thunderstorm from the altitudes of lightning emission sources. The key advantage of this approach over in situ balloon soundings is that lightning source altitudes can be measured remotely at considerable distances using Radio-Frequency (RF) sensors. Lightning Mapping Arrays (LMAs: Rison et al., 1999) are networks of Very High Frequency (VHF) band RF receivers that are capable of mapping the three-dimensional structure of lightning flashes with a nominal accuracy of tens of meters (Thomas et al., 2004) and a maximum range on the order of a few hundred kilometers (depending on the number of stations in the array and their geometry). The locations of individual charge layers manifest as local maxima in the VHF source altitude profile, while the polarity of each layer can be inferred from the relative frequency of sources (Rison et al., 1999). This is possible because lightning processes associated with a negative leader propagating through a positive charge layer are more prevalent emitters of VHF radiation than positive leaders propagating through a negative charge layer. Manual techniques and, more recently, automated routines like chargepol (Medina et al., 2021), use VHF source altitudes to characterize the bulk thunderstorm charge structure.

In addition to informing thunderstorm charge structures, lightning altitude measurements are also useful for revealing changes in updraft behavior (Fierro et al., 2011; Suszcynsky & Heavner, 2003) and quantifying the effects of lightning on atmospheric chemistry. Nitrogen oxides ($NO_x = NO + NO_2$) are a catalytic precursor in the photochemical production of tropospheric ozone (O_3) (Chameides & Walker, 1973; Crutzen, 1973; Crutzen et al., 1979; Seiler & Crutzen, 1980), which is an important greenhouse gas in the upper troposphere (Fishman et al., 1979; Lacis et al., 1990). Numerous sources contribute to the NO_X budget, including ground level sources such as biomass and hydrocarbon burning, and atmospheric sources including aircraft emissions and lightning (LNO_x). Ivanov et al. (2014) identified the temperature threshold for NO_x production to occur as 3000–4000 K. The lightning leaders that can be mapped with VHF measurements like LMAs typically have temperatures around 10000 K (Rakov & Uman, 2003). Thus, leaders are an important source of LNO_x, and the LNO_x output from individual flashes is expected to be concentrated at the altitudes where the leaders propagate. Multiple lightning altitude profiles have been created from either lightning measurements or parameterizations that can be used to estimate the LNO_x mass distribution for regional and global chemical transport models (Carey et al., 2016; DeCaria et al., 2000; Labrador et al., 2005; Luo et al., 2017; Mecikalski & Carey, 2018; Pickering et al., 1998; Tie et al., 2002). However, none of these profiles are representative of global lightning. The parameterizations rely on many assumptions about how lightning altitude scales with environmental parameters, while the measured profiles were created from regional 3D lightning mapping systems (LMAs and others) that have limited ranges and only cover certain land-based regions of the Earth that are heavily concentrated in the northern midlatitudes. Global lightning production, by contrast, is concentrated in the tropics (Albrecht et al., 2016; Cecil et al., 2014)—particularly in the "chimney" regions of South America, Africa, and the Maritime Continent (Williams & Sátori, 2004)—where 3D lightning measurements are sparse.

Altitude profiles of VHF lightning sources can also be derived from global space-based measurements. Jacobson et al. (1999) described a methodology for using the time delay between the VHF pulses produced by the direct line of sight measurement of an in-cloud lightning source and its reflection off the surface of the Earth to compute the altitude of the source. This method requires that the position of the satellite and the geographic location of the source be known. Light and Jacobson (2002) used this approach to generate VHF source altitude distributions for FORTE events coincident with either the National Lightning Detection Network (NLDN: Cummins et al., 1998) or FORTE's Optical Lightning System (Suszcynsky et al., 2001). The advantage of using joint RF/optical FORTE satellite observations to derive lightning altitude profiles is that its Low Earth Orbit (LEO) vantage point is not subject to the regional biases of the LMAs. However, Light and Jacobson (2002) only had a small sample on the order of 1,000 coincident lightning events available, which was not sufficient to examine variations in lightning altitude across the globe.

In this study, we apply the same approach as Jacobson et al. (1999) and Light and Jacobson (2002) to our comprehensive catalog of joint RF/optical FORTE detections to document lightning altitudes across the globe. This

initial overview of our new global lightning altitude data set will focus on regional and seasonal variations in the source altitude distribution and the altitudes of sources within lightning flashes. Future work will explore other applications of the FORTE lightning altitude data.

2. Data and Methodology

2.1. The FORTE Satellite

The FORTE satellite was launched into a nearly circular orbit with a 70° inclination and 825 km altitude in August 1997. It recorded both optical and VHF lightning events from 1997 until 2003, and optical only events until 2010. FORTE was unique not only for providing both optical and RF measurements of lightning from the same space-based platform, but also for being operated in a variety of modes. The FORTE instruments could be commanded to operate autonomously or to have one instrument trigger another; the record lengths and threshold settings could be changed; or individual instruments could be turned off, either entirely or at specific points in the FORTE orbit. The FORTE on-orbit commanding state evolved to meet the changing data collection needs of the science team over the FORTE mission. But, as a result, the FORTE data set is heterogeneous, with only a fraction of the lightning events recorded by FORTE having the coincident measurements from both the RF system and the OLS necessary for computing source altitude. The FORTE instruments that provide these joint measurements are summarized below.

2.1.1. The FORTE Optical Lightning System

The OLS consisted of two instruments: the Lightning Location System (LLS; Suszcynsky et al., 2000) and the Photodiode Detector (PDD; Kirkland et al., 2001; Suszcynsky et al., 2000). Both instruments had an 80° Field of View (FOV) and detected transient optical sources over a ∼1,200 km footprint on the surface of the Earth. The PDD recorded broadband (0.4–1.1 μm) optical waveforms from all activity across its circular FOV with a sampling interval of 15 μs and a variable record length that was most often 1.92 ms. The LLS, meanwhile, was a lightning imager whose role was to geolocate lightning events to within a nominal pixel (∼10 km) footprint. It was built from modified hardware from NASA's Lightning Imaging Sensor (LIS: Christian et al., 2000), with a front-end optical assembly and charge-coupled device (CCD) imaging array identical to LIS and an operations and signal processing module designed by Sandia National Laboratories.

Like LIS, the LLS operated autonomously and triggered whenever the signal amplitude in one of the pixels on its 128 × 128 imaging array integrated over a 2.47 ms frame exceeded a threshold above the background value. However, unlike LIS, flash clustering and background characterization were not performed, and thus could not inform the LLS signal processing. Consequently, the LLS did not take advantage of cluster-based energetic particle and glint filters like the LIS filters described in Christian et al. (2000). The LLS signal processing module did not screen for energetic particles, and the FORTE operators, instead, elected to turn the LLS off during certain orbits that took FORTE through the South Atlantic Anomaly (SAA). Moreover, a simple and severely limiting glint filter was implemented where individual LLS pixels would be turned off once they were illuminated for three-or-more consecutive frames. This prevented long-lasting lightning processes like Continuing Current (Bitzer, 2017 and references therein) that are prevalent in the LIS data from being well captured by the LLS.

2.1.2. The FORTE RF System

The FORTE RF system consisted of two different types of broadband VHF receivers: the "Two And Twenty Receiver" (TATR) and the "HUndred Megahertz Receiver" (HUMR). These receivers were connected to FORTE's two identical Log-Periodic Antennas that were mounted orthogonal to each other along the nadir-pointing boom (Jacobson et al., 1999; Light et al., 2001; Shao & Jacobson, 2001; Suszcynsky et al., 2000). TATR and HUMR recorded waveforms from global lightning from late 1997 until 2003 at various subbands within their broader 20–300 MHz VHF band.

The TATR payload consisted of two receivers (TATR-A and TATR-B) that would each sample one of the FORTE antennas. Each receiver could be independently tuned and would provide VHF measurements over hundreds of microseconds across a 22-MHz subband. In addition to tuning, TATR record lengths and the ratios of pre-trigger to post-trigger samples were also reconfigured throughout the FORTE mission, providing a heterogenous collection of VHF measurements. The HUMR payload consisted of a single receiver that sampled a wider 85 MHz

23335084, 2022, 9, Downloaded from https://agupubs.onlinelibrary.wiley.com/doi/10.1029/2022EA002404 by Los Alamos National Laboratory, Wiley Online Library on [11/10/2022]. See the Terms and Conditions (https://onlinelibrary.wiley.com/terms-and-conditions) on Wiley Online Library for rules of use; OA articles are governed by the applicable Creative Commons License

band. As with TATR, HUMR could be tuned to different frequency ranges across the VHF band. However, HUMR records were also generally longer than TATR records, lasting up to 6.75 ms.

The FORTE RF system had multiple triggering modes, including a manual trigger for on-orbit testing, an external trigger mode to capture RF waveforms from OLS events, and an autonomous trigger mode. These different modes are summarized in Light (2020). The autonomous trigger mode leveraged the wideband nature of lightning pulses to screen for terrestrial noise, which tends to be comprised of narrowband carrier signals. The wideband RF signal was divided into eight evenly spaced 1-MHz channels across the receiver passband. RF power was monitored in each of these channels, and an "alarm" was issued whenever the power in one of these channels exceeded a noise-riding threshold. If multiple channels (usually 5) produced simultaneous alarms, the RF system would trigger and record an event.

2.2. Signal Processing and Pulse Extraction

2.2.1. Generating Cluster Feature Data for FORTE

We previously constructed cluster feature data from FORTE events to compensate for the lack of flash level FORTE data in Peterson et al. (2021a, 2021b). Our FORTE feature data is modeled on the LIS science data described in Christian et al. (2000). FORTE events are clustered into "groups" that describe collections of events that arise from nominally the same pulse. Groups are clustered into features describing complete and distinct lightning flashes. Flashes are clustered into thunderstorm snapshots that are termed "areas," and periods of continuous emission in a single flash are described with "series" features.

There are three key differences between LIS and our FORTE data set. First, we use the larger OTD distance threshold of 16.5 km (Mach et al., 2007) to identify LLS groups in the same flash to accommodate its larger pixel footprint. Second, we employ the full fit clustering method used by the Geostationary Lightning Mapper (Goodman et al., 2012) that merges flashes in the scenario where a group occurs that could be assigned to multiple existing flashes. Third, we construct features for all three of FORTE's instruments, not just the imager. Our multisensor FORTE cluster feature data is produced for the entire data record from 1997 to 2010. We used it previously to identify interesting flashes in Peterson et al. (2021a, 2021b), and to generate event and flash statistics in Peterson (2022a, 2022c).

2.2.2. Extracting Sub-Event RF Features

The exceptional temporal sampling of the RF system and the PDD allow us to expand the cluster feature data tree to finer scales than events. The basic unit of RF/PDD clustering becomes microsecond-scale waveform samples. In the original clustering described in Peterson et al. (2021a, 2021b), we clustered samples into "pulse" features bounding contiguous portions of the waveform where the signal exceeded the background value by a specified threshold. This approach was applied directly to the PDD irradiance data and to the RF data after signal processing. The RF waveforms were first "prewhitened" to remove manmade carrier waves from the wideband measurements, and then "dechirped" to counteract the frequency-dependent delay in the signal time of arrival from propagation through the ionosphere. These standard procedures in FORTE analyses are described in Light (2020). RF pulses were then identified in the time series of average power across the band. For the TATR data, where we have two independent waveforms from each event, we used only the waveform with the greatest signal amplitude to extract pulses.

While this approach is sufficient for simple PDD and RF waveforms dominated by discrete high-amplitude pulses, it is not well-suited for distinguishing pulses in complex waveforms that contain multiple pulses of varying amplitude, spacing, and effective width (defined as total energy divided by peak power, as in Kirkland et al. (2001)). Therefore, we developed a new approach that could be applied to either the PDD or RF data to extract and characterize pulses over a variety of waveform shapes. Pulses and their child "peak" features are found by looping the pulse threshold from the maximum signal amplitude down to the noise threshold for the event. A new pulse feature is created when samples are found that both exceed the incremental threshold and do not occur within a specified time threshold of an existing pulse. If a new pulse is not identified, the existing pulses are expanded to include the new samples that exceed the incremental threshold. This new approach permits a single contiguous portion of the waveform that contains multiple prominent peaks separated in time to be partitioned into two or more pulse features. The old approach would always identify a single pulse feature in these complex waveforms.

23335084, 2022, 9, Downloaded from https://agupubs.onlinelibrary.wiley.com/doi/10.1029/2022EA002404 by Los Alamos National Laboratory, Wiley Online Library on [11/10/2022]. See the Terms and Conditions (https://onlinelibrary.wiley.com/terms-and-conditions) on Wiley Online Library for rules of use; OA articles are governed by the applicable Creative Commons License

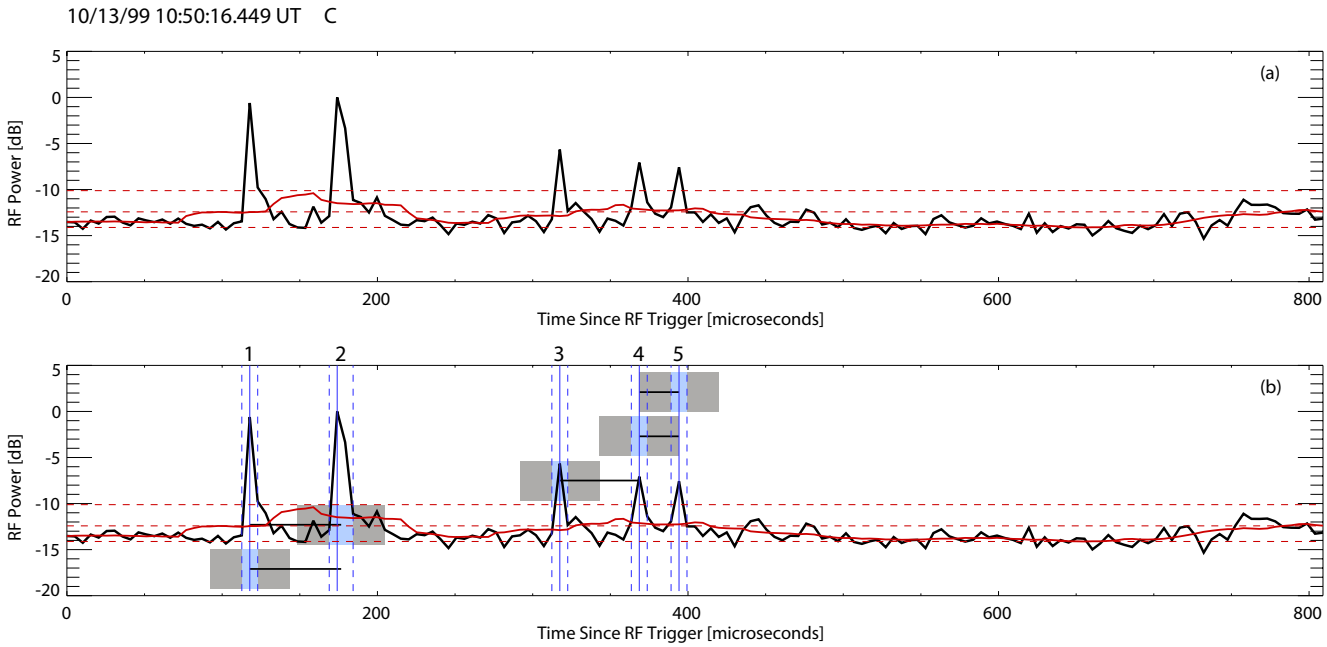

Figure 1. Example radio-frequency event record (a) with multiple identified pulses (b). Peak (solid blue vertical lines) and pulse (blue bars between dashed blue lines) features are identified from contiguous regions of the original power time series (black curve) that are three standard deviations (horizontal dashed lines) above the minimum of the smoothed time series (red curve), as described in text. Pulse windows used to compute their properties (gray bars) and links between pairs of impulsive events (horizontal black lines) are also shown.

To demonstrate pulse extraction, Figure 1 shows an example dechirped TATR waveform that contained two Trans-Ionospheric Pulse Pairs (TIPPs) from in-cloud lightning events and a third solitary pulse. The band-averaged power time series (solid black line) is first smoothed (solid red line), and the pulse feature threshold is determined as 3x the standard deviation above the minimum value in the smoothed curve (top dashed horizontal line). The iterative threshold method described above identifies five peak features (solid blue lines in Figure 1b) in 5 pulse features (blue bars with dashed vertical lines indicating their endpoints). Pulse characteristics are then computed using windows that encapsulate the pulse plus a 20 microsecond buffer on either side (gray boxes). Finally, TIPPs are identified as impulsive features that are in close temporal proximity to another impulsive feature. The constituent pulses in each TIPP are linked (solid horizontal black lines in Figure 1b), and the peak-to-peak time difference for the TIPP is recorded.

In TIPP cases where multiple candidate links might be made (as with pulses 3 and 4 in Figure 1b), feature links are prioritized by minimizing a Weighted Euclidean Distance (WED) function of the differences in time and feature attributes (i.e., pulse width, peak power, rise time, etc.). In Figure 1b, Pulse 3 was linked to Pulse 4 because it produced the lowest WED values of the remaining features, even though Pulse 4 was a better match for Pulse 5. A common cause of these differing links is that only one of the pulses in the TIPP exceeds the noise threshold, which appears to be the case here. To mitigate this potential source of uncertainty in the pulse separation times, we only consider TIPPs where both constituent pulses identify the other as its partner, as with Pulse 4 and Pulse 5. The two pulses that comprise each linked TIPP are merged into a single entry in our feature database.

Applying these methods to all types of RF events in the FORTE record produces the pulse statistics shown in Figure 2. Events whose power time series were too flat to produce any pulse features are not considered. Most of the remaining events contain only 1 or 2 pulses (Figure 2a)—with a peak at 2 due to the prevalence of TIPPs in the data. However, the remaining 40%–50% events (depending on the category) contain more than 2 pulses. These may be trains of weak TIPPs from in-cloud lightning events, a Cloud-to-Ground (CG) stoke with a TIPP, or a diffuse in-cloud event (i.e., a K-change) with embedded impulsive events. The longer events in the FORTE RF record that last multiple milliseconds can contain dozens of distinct pulses. The number of individual peaks in a given pulse (Figure 1b) also varies by pulse type. Nominally, each pulse will have a single peak per pulse (or 2 peaks per TIPP). However, 17% of pulses have 3-or-more peaks. Analyzing these events (not shown for brevity)

23335084, 2022, 9, Downloaded from https://agupubs.onlinelibrary.wiley.com/doi/10.1029/2022EA002404 by Los Alamos National Laboratory, Wiley Online Library on [11/10/2022]. See the Terms and Conditions (https://onlinelibrary.wiley.com/terms-and-conditions) on Wiley Online Library for rules of use; OA articles are governed by the applicable Creative Commons License

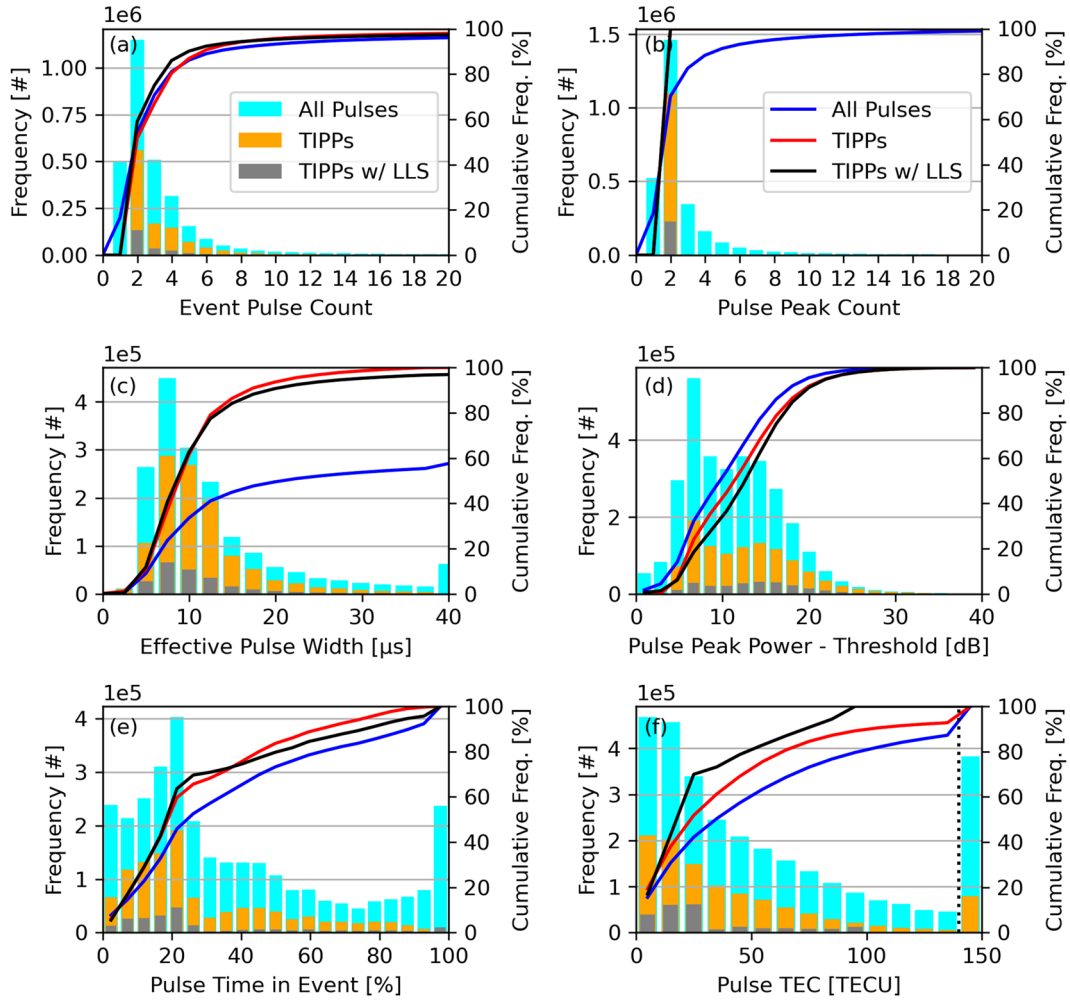

Figure 2. Histograms and cumulative distributions of (a) the number of pulses per event, (b) the number of peaks per pulse, (c) the effective pulse with, (d) the peak power above the threshold, (e) the time of the pulse in the event record, and (f) the total electron content experienced by the pulse reported by the dechirping algorithm. Separate distributions are shown for all pulses, trans-ionospheric pulse pairs (TIPPs), and TIPPs that also have lightning location system coincidence at the flash level.

indicates that they tend to be mixed events where the peaks (including TIPPs) were not sufficiently isolated in time from the other nearby peaks to create separate pulse features.

Pulse features also have a wide range of effective widths (Figure 2c). The median effective width for an individual pulse in a TIPP is 8 μs, and the frequency of TIPPs in the FORTE data heavily biases the general pulse width statistics. Only ∼40% of general pulses in our database have effective widths exceeding 40 microseconds, with the peak at 40 microseconds being artificial due to the thresholds used in the algorithm. These thresholds also control the minimum signal amplitude that results in a pulse being identified (Figure 2d). Few general pulses and hardly any TIPPs are resolved with a peak amplitude <2 dB above the noise threshold. Most pulses exceed the threshold by at least 5 dB. Pulses like Pulse 1 and 2 in Figure 1b are more common in our data set than Pulses 4 and 5 because the threshold is set fairly high compared to the actual noise floor in order to reduce the number of spurious events. This also means that, while we do not restrict our sample to low band (20–50 MHz) TATR detections, these events dominate because lightning is more powerful in the low band and the HUMR waveforms tend to be noisier than TATR waveforms.

These pulses also occurred throughout the RF event waveform record (Figure 2e). The most common location in the record was around 25% of the record length, with increased frequencies earlier in the record compared to later. This is due to both the commanded pretrigger fraction and the dechirping process pushing the signal back

23335084, 2022, 9, Downloaded from https://agupubs.onlinelibrary.wiley.com/doi/10.1029/2022EA002404 by Los Alamos National Laboratory, Wiley Online Library on [11/10/2022]. See the Terms and Conditions (https://onlinelibrary.wiley.com/terms-and-conditions) on Wiley Online Library for rules of use; OA articles are governed by the applicable Creative Commons License

23335084, 2022, 9, Downloaded from https://agupubs.onlinelibrary.wiley.com/doi/10.1029/2022EA002404 by Los Alamos National Laboratory, Wiley Online Library on [11/10/2022]. See the Terms and Conditions (https://onlinelibrary.wiley.com/terms-and-conditions) on Wiley Online Library for rules of use; OA articles are governed by the applicable Creative Commons License

Table 1
Variations in Radio-Frequency Pulse Feature Counts After Successively Applying Each Filter

	All pulses	TIPPs	TIPPS w/LLS coincidence
No filters	3,089,812	1,096,885	380,347
Valid TEC	2,694,726	1,006,466	330,302
Centered in record	2,437,408	907,083	300,214
Isolated in time	1,796,217	695,146	202,062
1 Active LLS area	-	-	152,955
1 Active LLS flash	-	-	130,261

Note. The final two filters are only applied for the analyses in Section 3.3 and the Supporting Information S1.

to its vacuum time of arrival. Higher Total Electron Content (TEC) values along the slant path taken by the signals through the ionosphere will result in larger temporal displacements than lower TECs. This can pose a problem for characterizing pulses at the beginning of the RF record. The initial portion of a broader pulse or the first constituent pulse of an early TIPP can be computationally rolled to the end of the record by the dechirping algorithm. This is why there is a second peak in Figure 2e at the end of the record. It is not physical, but rather an artifact of dechirping.

Pulses traversing the ionosphere along paths with high TEC values were observed by FORTE due to its global observation domain and large effective FOV (Figure 2f). Our identified pulses were subject to TEC values ranging from near 0 TEC units (TECU) to greater than 120 TECU (Figure 2f). Moreover, the dechirp algorithm failed in certain events, while there were other events that resulted from onboard discharges on the spacecraft. Both of these scenarios yield a reported TEC ≤0 TECU and are shown in the rightmost bin in Figure 2f.

2.3. Filtering LLS-Coincident RF Events

The pulse statistics in Figure 2 indicate that we can use automated routines to create a robust sample of distinct RF pulses from the FORTE data. However, these pulses need to be filtered to ensure that the VHF source altitudes are physically meaningful. Pulses that lack LLS coincidence will not be useful. Meanwhile, pulses that occur at the beginnings or ends of the record, or that report a TEC ≤0 TECU, will yield questionable pulse time differences.

However, the FORTE sampling of global pulses is already uneven—due in large part to the heterogeneous FORTE commanding—and filtering the RF data further impacts the global distribution of detected VHF sources. Table 1 summarizes the pulse counts in our global sample. In total, three million distinct pulses are identified including, one million TIPPs (36% of all pulses). Figure 4 shows global distributions of RF events with pulse features (Figure 4a), all RF pulse features (Figure 4b), and RF TIPPs (Figure 4c) according to the FORTE satellite subpoint. While FORTE detections of the pulses in Table 1 are generally concentrated in the tropics, and particularly around the tropical chimneys in the Americas, Africa, and the Maritime Continent, all three global source distributions differ substantially from lightning climatologies derived from NASA sensors in Cecil et al. (2014), Albrecht et al. (2016), and Peterson et al. (2021c). Perhaps the most notable departures occur in Africa, where VHF sources are prevalent in West Africa while being infrequent in the primary lightning hotspot on the continent, in the Congo Basin. Additionally, horizontal banding can be noted in the Indian Ocean and Asia where RF detections are concentrated within a specific latitude range surrounding the equator. A second band is also apparent in the Southern Ocean. These bands are not natural, but result from FORTE commanding.

LLS coincidence is required to compute source altitude, but this requirement convolutes the sampling biases of the two sensors. To minimize these biases to the extent possible while preserving a reasonable sample size, we elect to take a "flash-level" approach to defining LLS coincidence. Following the FORTE clustering scheme, we consider all LLS events that occur within 330 ms of the RF pulse to be candidates for the location of its origin. We compute this location as the radiance-weighted mean position of all events in the time window. Under normal circumstances, all of these events would come from the same parent flash—or at least the same parent thunderstorm area—and the RF source would be geolocated to a point within 10–30 km of its true location. However, it is possible to have multiple ongoing thunderstorms producing events within the LLS FOV at the same time. When this occurs, the RF source location is weighted toward the more active thunderstorm.

Of the original one million RF TIPPs, the flash level LLS coincidence requirement limits the sample size to 380,000. These are the "TIPPs with LLS" entries in Figure 2. LLS-coincident TIPPs have similar effective width statistics to normal TIPPs (Figure 2c), are somewhat more powerful (Figure 2d), and their times similarly peak at 25% of the record length (Figure 2e), indicating that they were commonly the triggering pulse. However, their slant TECs in Figure 2f are significantly lower than the 20–30 TECU medians for the other pulse categories. This is due to two known biases imposed by the LLS: (a) the smaller 80° LLS FOV removes events that originate near the limb and traverse nearly horizontally through the ionosphere (experiencing high TECs) from the sample, and

23335084, 2022, 9, Downloaded from https://agupubs.onlinelibrary.wiley.com/doi/10.1029/2022EA002404 by Los Alamos National Laboratory, Wiley Online Library on [11/10/2022]. See the Terms and Conditions (https://onlinelibrary.wiley.com/terms-and-conditions) on Wiley Online Library for rules of use; OA articles are governed by the applicable Creative Commons License

(b) the LLS being more capable of detecting lightning at night (when TECs are low) compared to during the day (when TECs are high). Diurnal performance differences were also an issue with LIS that had to be compensated for when creating the global lightning flash rate climatologies (Albrecht et al., 2016; Cecil et al., 2014; Peterson et al., 2021c).

If we exclude pulses that have invalid TECs or that occur in the first or last 5% of the record, we are left with 2.4 million events, 907,083 of which (37%) are TIPPs. Of these TIPPs, 300,214 have LLS coincidence at the flash level. Finally, if we further exclude pulses that occur within 100 microseconds of another pulse (like Pulse 3 in Figure 1), the sample size is reduced to 1.8 million pulses and 695,146 TIPPs (39%), 202,062 of which have LLS coincidence. We can also optionally require that only a single LLS flash or LLS area is active at the time of the RF event. This further reduces the sample to 152,995 LLS-coincident TIPPs at the area level and 130,261 LLS-coincident TIPPs at the flash level. This filtering leaves us with 100–200 k TIPPs from across the globe that we can use to compute the VHF source altitudes, a sample that is two orders of magnitude larger than Light and Jacobson (2002).

2.4. Calculating the Altitudes of Global VHF Sources

Jacobson et al. (1999) derived the following equation for the altitude of the VHF source responsible for a TIPP:

$$a = c \cdot \tau \frac{\sin \beta}{1 - \cos 2\beta} \quad (1)$$

where c is the speed of light, τ is the time delay between the pulses that comprise the TIPP, and β is the satellite elevation angle, which can be computed from the satellite position and the latitude and longitude of the source. This equation assumes a spherical Earth where the source is close to the surface.

Our use of flash level LLS coincidence to geolocate the source is only justified as long as the location errors from geolocating to the wrong part of the storm or flash (i.e., a few tens of kilometers) only result in small altitude errors. To test this, we compute the altitude of a TIPP with a 20 μs pulse separation at each point across the LLS FOV in Figure 4a and the altitude error that would result from the TIPP being offset 10 km radially outward from its true position in Figure 4b. Within the limited 80° LLS FOV, the maximum error in altitude for being displaced by 10 km is only expected to be around 60 m. Therefore, we can be off by even a few tens of kilometers without observing a notable effect on the altitude statistics.

The key parameter to measure precisely is the time difference between the two peaks in the TIPP. Figure 4c computes the altitude error from being off by just 1 μs for a source at each point on the LLS imaging array. Each microsecond of error results in an altitude error of between 150 m at nadir and 350 m at the edge of the LLS FOV. It only takes a 3 microsecond error for an edge source to be displaced in altitude by a full kilometer.

3. Results

The following sections will document the FORTE distributions of lightning altitudes derived from LLS-coincident VHF source data. Section 3.1 will examine global distributions of VHF source altitude. Section 3.2 will consider variations in the lightning altitude profiles between different regions of the Earth and across the seasons. Finally, Section 3.3 will examine the VHF source altitude distributions in LLS flashes.

3.1. Global Distributions of the Altitudes of VHF Lightning Sources

The FORTE orbit covered all of the major lightning-producing regions of the Earth, but these regions were not sampled consistently, as we saw in the global distributions of RF events and pulses in Figure 3. These biases are compounded by requiring LLS coincidence, which substantially (see Table 1) and unevenly reduces the number of events considered. The global distribution of LLS-coincident RF TIPPs is shown in Figure 5. Figure 5a is analogous to the plots from Figure 3, except the FORTE satellite subpoint location is replaced with the geolocated LLS source location. The same RF event hotspots in the Americas, West Africa, and the Maritime Continent can

10.1029/2022EA002404

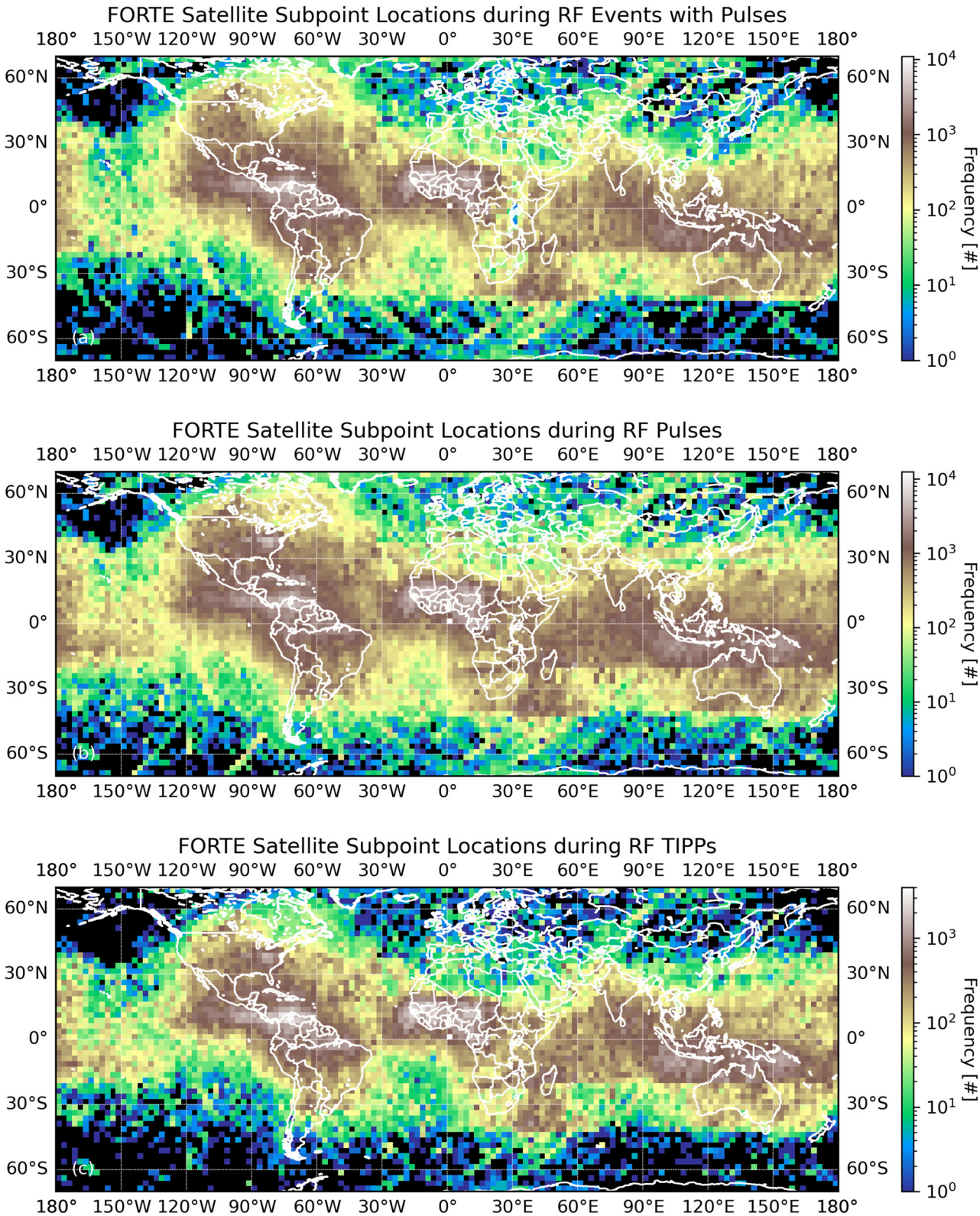

Figure 3. Global distributions of the fast on-orbit recording of transient events satellite subpoint position for (a) radio-frequency (RF) events containing pulse features, (b) RF pulse features, and (c) RF trans-ionospheric pulse pairs.

23335084, 2022, 9, Downloaded from https://agupubs.onlinelibrary.wiley.com/doi/10.1029/2022EA002404 by Los Alamos National Laboratory, Wiley Online Library on [11/10/2022]. See the Terms and Conditions (https://onlinelibrary.wiley.com/terms-and-conditions) on Wiley Online Library for rules of use; OA articles are governed by the applicable Creative Commons License

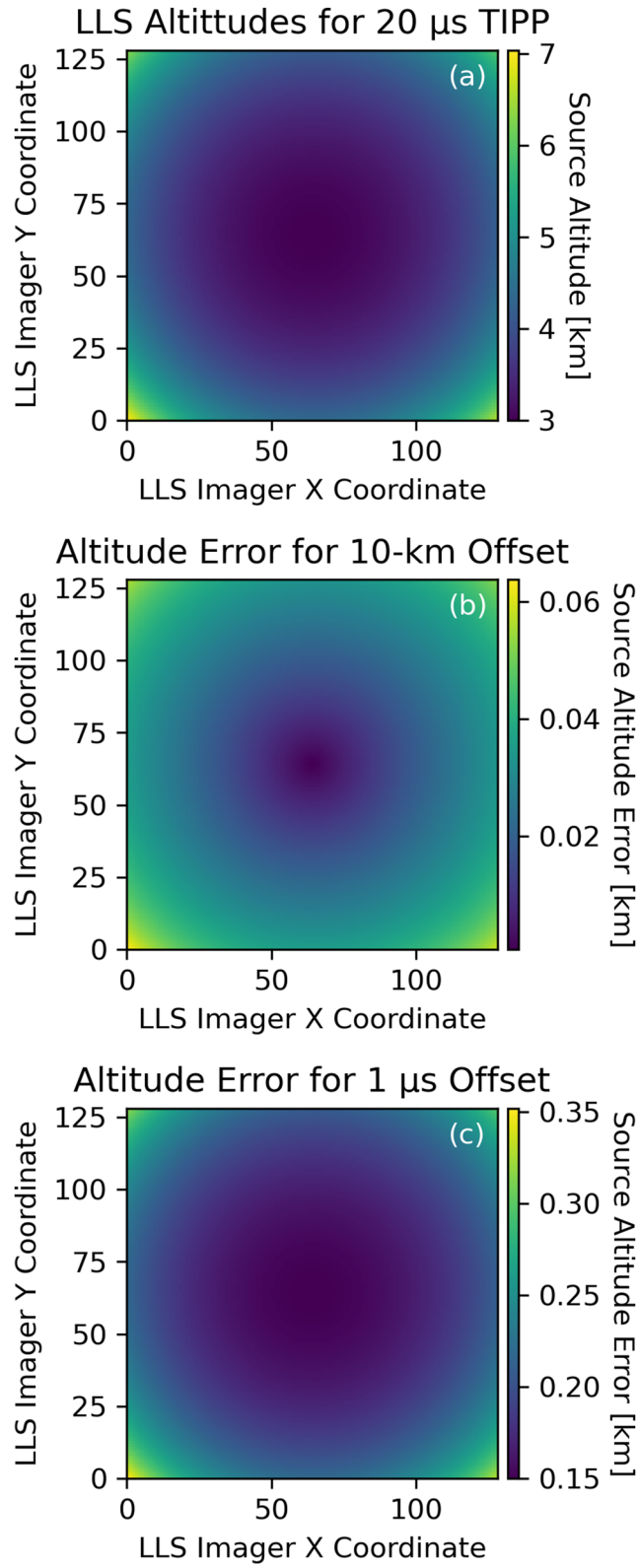

Figure 4. Distributions of (a) altitude and (b) and (c) altitude error for a trans-ionospheric pulse pair with a 20 µs intra-pulse time interval located at each lightning location system imager pixel. (b) The altitude error from the detected very high frequency source being displaced 10 km radially outward from its true location. (c) The altitude error from the intra-pulse time interval being off by 1 µs.

23335084, 2022, 9, Downloaded from https://agupubs.onlinelibrary.wiley.com/doi/10.1029/2022EA002404 by Los Alamos National Laboratory, Wiley Online Library on [11/10/2022]. See the Terms and Conditions (https://onlinelibrary.wiley.com/terms-and-conditions) on Wiley Online Library for rules of use; OA articles are governed by the applicable Creative Commons License

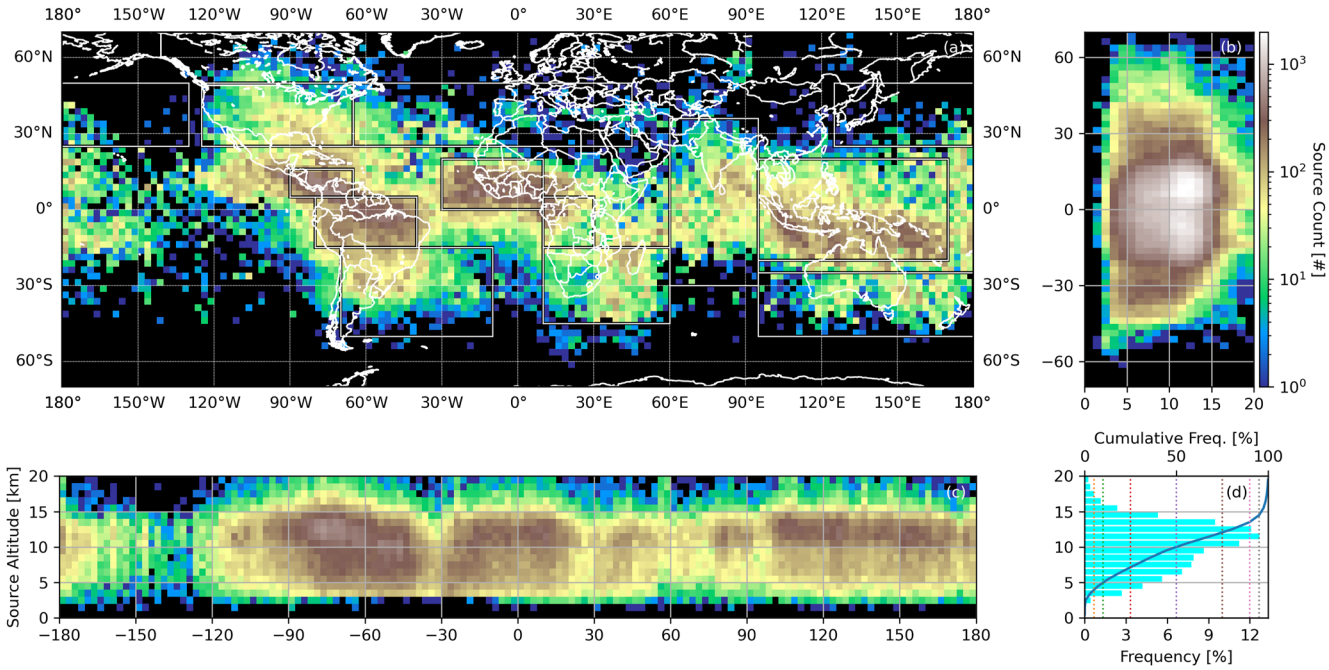

Figure 5. Distributions of lightning location system-coincident very high frequency (VHF) sources. (a) Geographic distribution of VHF sources with regions of interest boxed. (b) Latitude-altitude source distribution. (c) Longitude-altitude distortion. (d) Global source altitude histogram (bars) and cumulative distribution (solid line).

be noted, but the LLS coincidence requirement removes the horizontal banding in the distribution while limiting the number of samples at middle- and high-latitudes (particularly over the Eurasian continent).

Source altitude distributions by latitude (Figure 5b) and longitude (Figure 5c) are shown to the right of and below the global distribution in Figure 5a, while the global altitude profile is plotted in Figure 5d. Source altitudes are dominated by the upper charge layer at 10–12 km altitude, which is normally positively charged in the tripole thunderstorm model. The VHF source peak at high altitudes in the storm is consistent with negative leader propagation through a positive charge region, as negative leaders are good emitters of VHF radiation. Light and Jacobson (2002) also identified peaks in their VHF emitter altitude profiles in this range. Lower-altitude sources are less frequent and are usually found between 5 and 10 km.

However, not all regions conform to the global profile in Figure 5c, and some regional differences can be noted in the global latitude (Figure 5b) and longitude (Figure 5c) distributions. Low-altitude sources are more common over the longitude range associated with the Americas chimney compared to the Maritime Continent chimney region. While the African chimney in the Congo Basin is not well resolved, the West Africa maximum has a greater proportion of low-altitude sources along the west African coast compared to in the east of the continent. The source distributions also tend to be taller at low latitudes near the equator in Figure 5b compared to the midlatitudes, where a subtle low-altitude peak at 6 km altitude is faintly visible.

3.2. Regional and Seasonal Variations in Lightning Altitude

Due to the uneven sampling of the data, we will focus our discussion around altitude profiles that have first been normalized by the local event count. Twelve global regions are boxed in Figure 5a that roughly correspond to the northern hemisphere midlatitudes, the northern hemisphere tropics, the southern hemisphere tropics, and the southern hemisphere midlatitudes for the three continental chimneys: the Americas, Europe and Africa, and Asia. The VHF source altitude profiles for each of these regions are shown in Figure 6 organized horizontally by longitude and vertically by latitude.

The source altitude distributions in these regions differ from the global altitude profile in Figure 5d. The continental United States (Figure 6a) has a pronounced plateau between 5 and 10 km similar to the NLDN-matched profile in Light and Jacobson (2002). The other midlatitude regions such as South Africa (Figure 6k) and

23335084, 2022, 9, Downloaded from https://agupubs.onlinelibrary.wiley.com/doi/10.1029/2022EA002404 by Los Alamos National Laboratory, Wiley Online Library on [11/10/2022]. See the Terms and Conditions (https://onlinelibrary.wiley.com/terms-and-conditions) on Wiley Online Library for rules of use; OA articles are governed by the applicable Creative Commons License

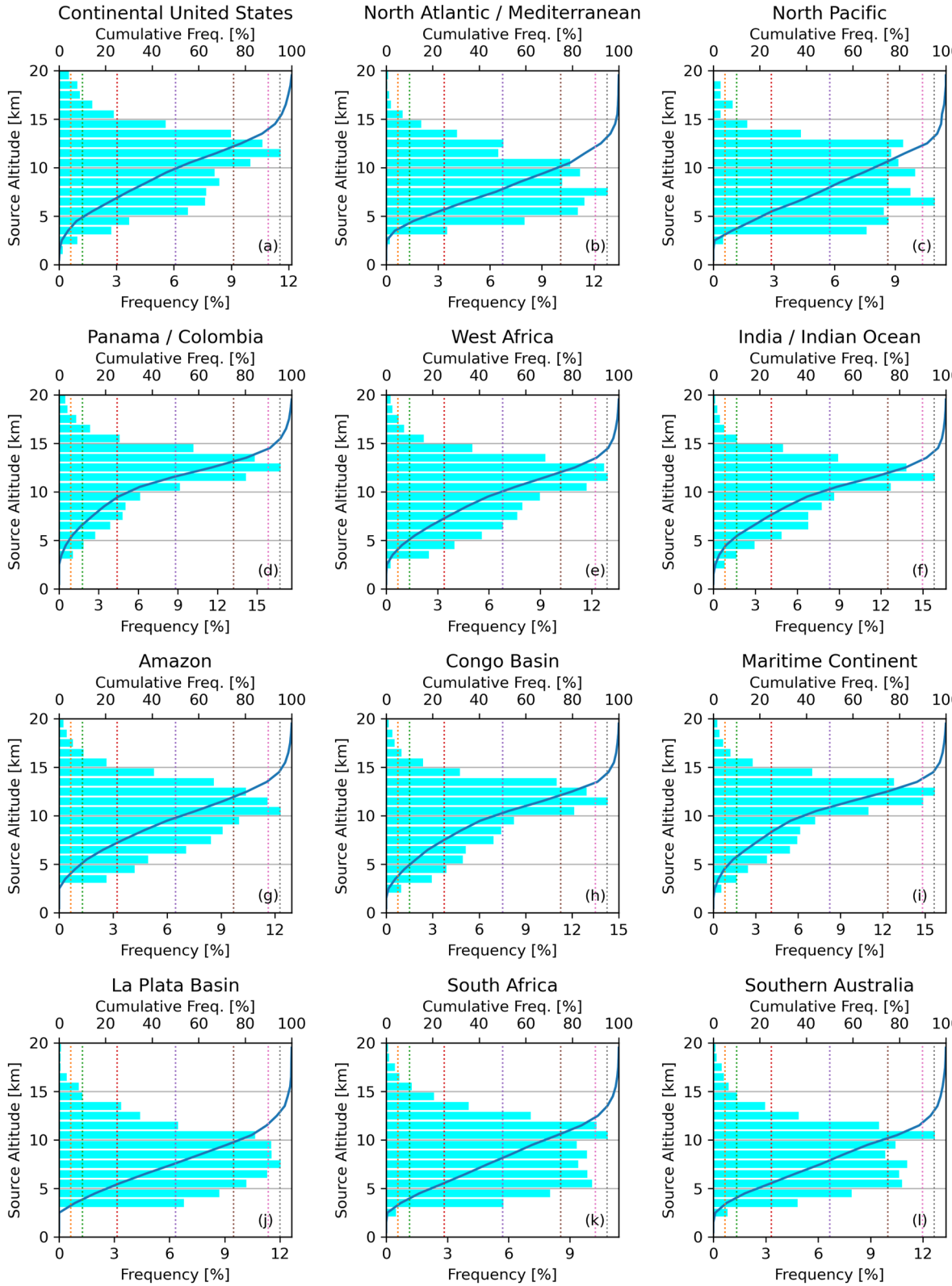

Figure 6. Very high frequency source altitude profile for the regions boxed in Figure 5 organized by longitude (columns) and latitude (rows).

23335084, 2022, 9, Downloaded from https://agupubs.onlinelibrary.wiley.com/doi/10.1029/2022EA002404 by Los Alamos National Laboratory, Wiley Online Library on [11/10/2022]. See the Terms and Conditions (https://onlinelibrary.wiley.com/terms-and-conditions) on Wiley Online Library for rules of use; OA articles are governed by the applicable Creative Commons License

23335084, 2022, 9, Downloaded from https://agupubs.onlinelibrary.wiley.com/doi/10.1029/2022EA002404 by Los Alamos National Laboratory, Wiley Online Library on [11/10/2022]. See the Terms and Conditions (https://onlinelibrary.wiley.com/terms-and-conditions) on Wiley Online Library for rules of use; OA articles are governed by the applicable Creative Commons License

southern Australia (Figure 6l) also have enhanced activity at low altitudes, and low-level activity even dominates in midlatitude regions where a large fraction of the sources come from over the ocean—including the North Atlantic/Mediterranean Sea (Figure 6b) and the northern Pacific Ocean (Figure 6c). The La Plata basin is distinct because its thunderstorms form over land where they can grow upscale into large Mesoscale Convective Systems (MCSs) before moving offshore. Its altitude profile is heavily weighted toward low-altitude sources, with a peak at 7 km. However, this is not solely due to the contribution of oceanic thunderstorms. When the oceanic sources are removed, the peak only increases to 8 km altitude.

There are a few potential explanations for why the La Plata basin has such a low source altitude profile. The most problematic cause would be contamination from SAA artifacts generating errors in the LLS source locations. SAA artifacts manifest as single-pixel detections or detections along a streak of pixels. These are random and isolated in time to an instrument like the LLS. Due to this randomness, they are not expected to consistently displace the source location toward the center of the array, where the altitude corresponding to a given intra-pulse time difference would be lower (i.e., Figure 4a).

However, other LLS hardware errors potentially caused by the SAA can generate anomalously high event counts at the center of the imaging array. We can account for this possible source of error by not considering the LLS and instead plotting the RF intra-pulse time for each TIPP. When we replace source altitude in Figure 6 with the intra-pulse time (not shown for brevity), the La Plata basin altitude profile also has smaller time delays between pulses, consistent with a greater share of low-altitude sources compared to other regions. Therefore, the altitude profile in Figure 6j appears to be legitimate and not due to SAA contamination.

We suggest that these increased fractions of low-altitude sources in certain regions is caused by lightning occurring in thunderstorm regions that do not conform to the tripole model: particularly electrified stratiform clouds. VHF-radiant negative leaders propagate through regions of positive charge in both convective and nonconvective clouds. While this propagation is confined to a small area in convective cases, stratiform flashes can propagate over hundreds of kilometers (Lang et al., 2017; Lyons et al., 2020; Peterson, 2019). Our previous analysis of an oceanic megaflash in the FORTE record showed that the flash constantly emitted VHF radiation in multiple periods of sequential triggering (i.e., series) that each lasted tens to hundreds of milliseconds. The impulsive VHF sources that we could identify were clustered in a single vertical layer between 4 and 8 km altitude (Peterson et al., 2021a). While megaflashes occur in many regions, the La Plata basin is one of the primary Americas hotspots (Peterson, 2021; Peterson & Stano, 2021)—along with the Continental United States, which also has an increased share of low-altitude sources in Figure 6a. We have also recorded long horizontal lightning over the Mediterranean Sea (Peterson, Rudlosky, & Deierling, 2017) (Figure 6b) and showed that the other midlatitude oceanic regions with increased low-altitude source fractions in Figure 6 are locations with long horizontal flashes (Figure 5 in Peterson, Deierling, et al., 2017).

The tropical regions in Figure 6, by contrast, are more heavily weighted toward higher altitudes. However, the source altitude profiles still differ between these tropical regions. If we rank these regions by the 75th percentile VHF source altitude, Panama/Colombia (Figure 6d) has the overall tallest thunderstorm charge structures (13.6 km), followed by the Maritime Continent (Figure 6i; 13.0 km), the Continental United States (12.6 km), and then the Congo Basin (Figure 6h; 12.6 km) and West Africa (Figure 6e; 12.5 km). The Amazon Basin (Figure 6g) has a nearly identical 75th percentile source altitude as the joint India/the Indian Ocean region (Figure 6f) of 12.4 km. The Amazon has a larger share of low-altitude sources and, despite this higher 75th percentile altitude, the mode is only at 10 km altitude.

Figure 7 maps these 75th percentile source altitudes (Figure 7a) for each grid point in Figure 5 along with the median (Figure 7b) and 25th percentile (Figure 7c) values. Pixels with less than 10 sources are not shown. The large regional domains used in Figure 6 obscure the fine-scale structure caused by thunderstorm interactions with the local terrain. Tropical oceanic thunderstorms over the Caribbean Sea, Gulf of Mexico, Indian Ocean, and Pacific Ocean can be as tall as land-based storms. At the same time, oceanic storms at higher latitudes (and in the Atlantic Ocean between the Americas and Africa) tend to be quite shallow.

Much of the midlatitude behavior is due to seasonal trends. Figure 8 shows latitude-altitude profiles for land, the coastal ocean (within 1,000 km of the continents), and the open ocean (beyond 1,000 km) averaged over 3-month periods. The profiles for each latitude are normalized according to the total number of detected sources such that all columns in each panel sum to 100%. The land-based source altitude profiles (left column) extend up to high

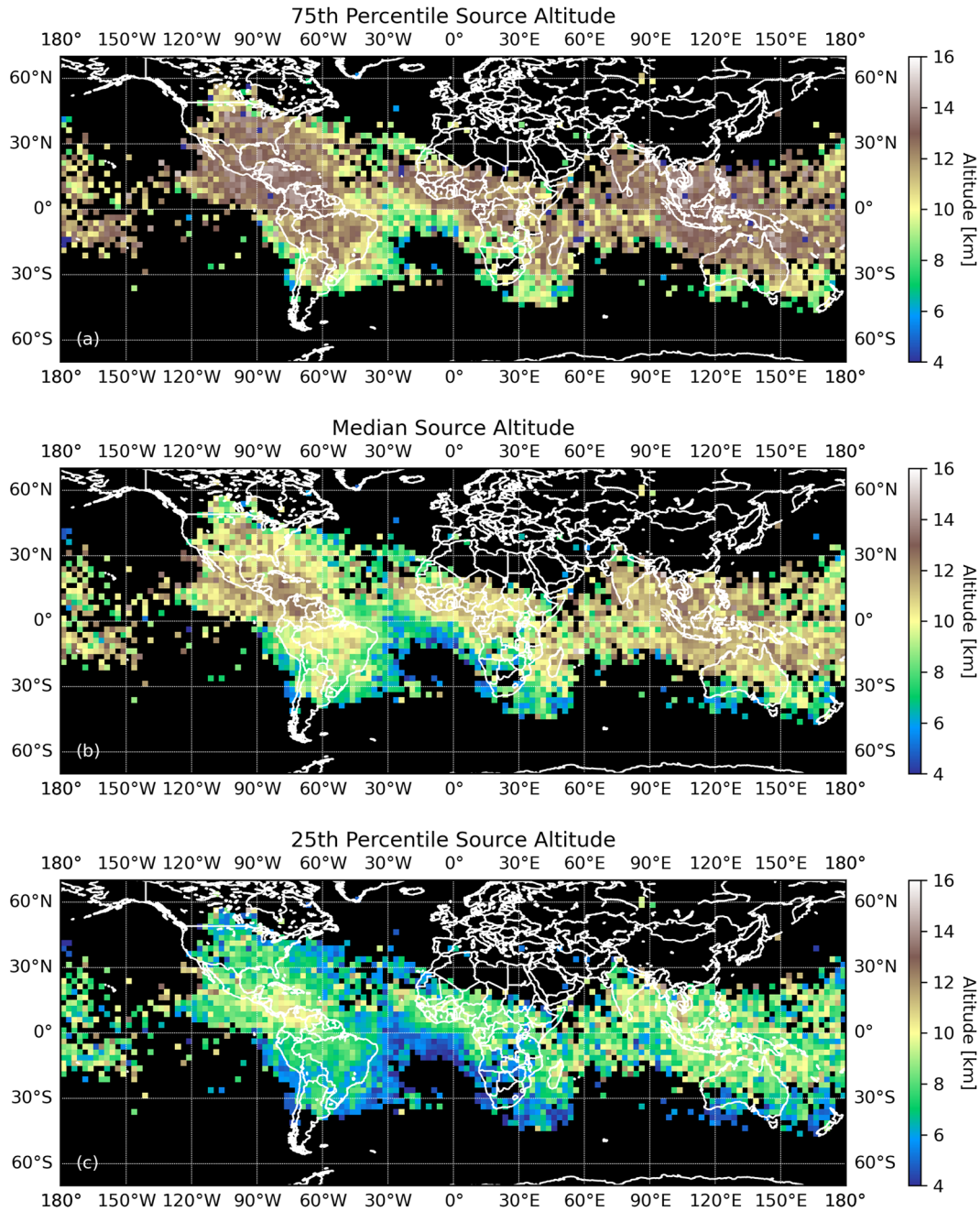

Figure 7. Global maps of (a) 75th percentile, (b) median, and (c) 25th percentile source altitudes.

altitudes during the summer season with a dominant upper positive charge layer above 10 km. During the winter, source altitudes are concentrated at lower altitudes around of 5 km. The passing of the seasons causes the summer upper and winter lower maxima to move in latitude according to changes in insolation. The apparent slant in the distribution during northern hemisphere fall, winter, and spring is due to the prevalence of low-altitude sources in the southern hemisphere (i.e., La Plata, South Africa, and Southern Australia) regions discussed previously. The coastal ocean profiles, meanwhile, are similar to their land-based counterparts, and we can also see similar seasonal behavior with the open ocean profiles (right column), though data is sparse from these low flash rate thunderstorms far from shore.

23335084, 2022, 9, Downloaded from https://agupubs.onlinelibrary.wiley.com/doi/10.1029/2022EA002404 by Los Alamos National Laboratory, Wiley Online Library on [11/10/2022]. See the Terms and Conditions (https://onlinelibrary.wiley.com/terms-and-conditions) on Wiley Online Library for rules of use; OA articles are governed by the applicable Creative Commons License

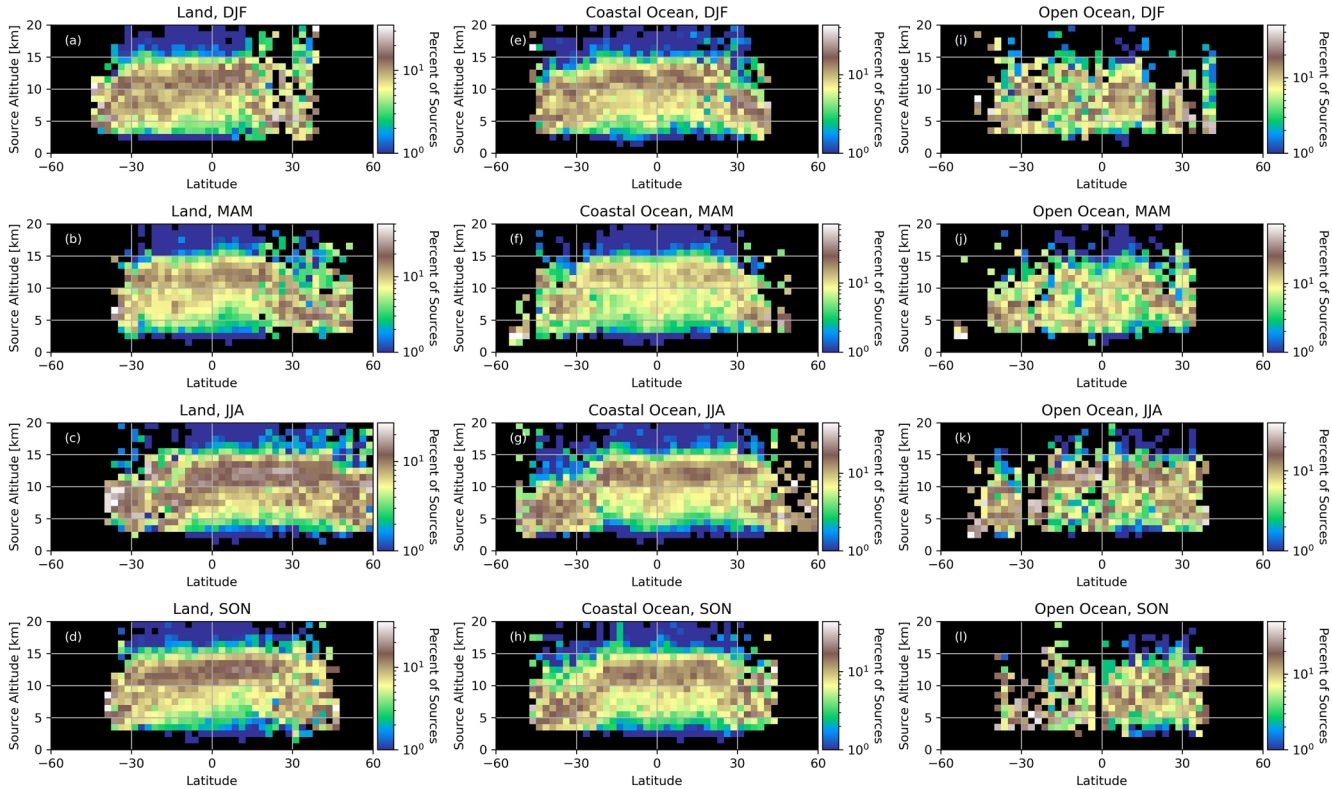

Figure 8. Latitude-altitude distributions of very high frequency sources detected over land (left), the coastal ocean (center), and the open ocean (right) during December–February (top row), March–May (second row), June–August (third row), and September–November (bottom row).

3.3. Source Altitudes in LLS Flashes

We previously demonstrated that FORTE is capable of documenting the three-dimensional propagation of individual flashes in Peterson et al. (2021a, 2021b). However, as we were unable to reliably extract pulses and peak times, we applied the source altitude algorithm by hand. In this section, we will use the new automated FORTE-derived altitudes in our cluster feature data set to examine how intracloud (IC) source altitudes vary within flashes.

An example of a particularly well-resolved flash is shown in Figure 9. Source altitudes before (Figure 9a), during (Figure 9b), and after (Figure 9c) the flash of interest are shown in blue for the flash and in red for other flashes. We normally only consider isolated sources that do not have pulses within 100 microseconds of the TIPP. However, to provide a more complete picture of VHF activity in this particular flash, we show these potentially ambiguous sources in black in Figure 9b. The extent of the LLS flash at each point in time is also overlaid as a line plot. VHF sources are mapped in Figure 9d and colored according to whether they occurred in the flash of interest and whether they occurred above or below 9 km altitude. Finally, a source altitude distribution is shown in Figure 9e.

The flash in Figure 9 occurred in a thunderstorm over the Pacific Ocean on 12/7/2001. It started with an RF-powerful TIPP at 7 km altitude followed promptly by activity in the upper positive layer that was resolved by the LLS (line in Figure 9b). If we assume that these initial sources bound negative leader breakdown, then the approximate vertical speed of the developing leader would have been 6.2×10^5 ms^{-1}. Infrequent activity can also be noted in a lower (apparently negative) layer around 6 km altitude, as well as between the two layers. Since the first source in the lower layer was ambiguous (black in Figure 9b), our filtered data set would identify the initial activity in this layer as occurring 300 ms into the flash. The low frequency of sources from the lower negative layer causes reductions in source counts from ambiguous events to have a greater impact on our statistics than for the upper positive layer. There were no other flashes before the flash of interest, but a few were detected in the 30 s after it ended. These flashes occurred in two thunderstorm areas to the north of the flash of interest. One is visible in Figure 9d, while the other was located on the other side of the LLS FOV. These other flashes had similar

23335084, 2022, 9, Downloaded from https://agupubs.onlinelibrary.wiley.com/doi/10.1029/2022EA002404 by Los Alamos National Laboratory, Wiley Online Library on [11/10/2022]. See the Terms and Conditions (https://onlinelibrary.wiley.com/terms-and-conditions) on Wiley Online Library for rules of use; OA articles are governed by the applicable Creative Commons License

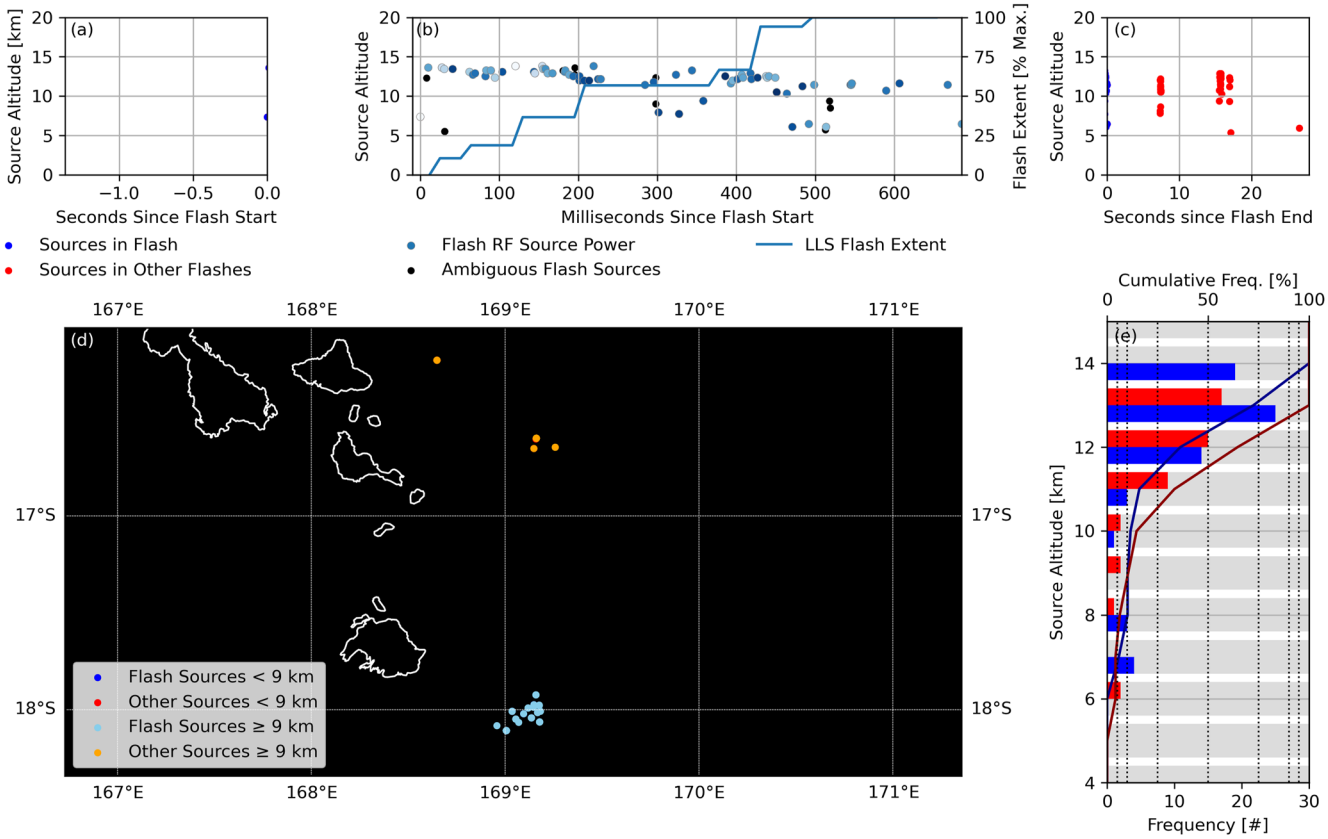

Figure 9. Altitude time series of source altitudes (a) before, (b) during, and (c) after an lightning location system flash of interest. Sources that were part of the flash are shown in blue, while sources in other flashes are shown in red. The locations of these sources are mapped in (d), and their vertical profiles are shown in (e). The blue color scale in (b) denotes radio-frequency power from minimum (dark blue) to maximum (white). Sources with ambiguous trans-ionospheric pulse pair links are denoted with black in (b). Sources in (d) are shaded according to altitude.

altitude profiles (Figure 9e) to the flash of interest, with a high concentration of sources around 12 km altitude and a comparably few low-altitude sources.

Our analyses of FORTE flashes in Figure 9 and in Peterson et al. (2021a, 2021b) demonstrate that automatically resolving thunderstorm charge structure with algorithms like chargepol is feasible for space-based platforms. This was even shown in Figure 21 Jacobson et al. (1999), though a lack of geolocation information meant that the flash evolution was mapped in units of TIPP intra-pulse time rather than altitude. However, there will be difficulties in applying these methods to on-orbit data. The first issue is view time. Chargepol accumulates LMA data over time to derive the bulk electrical structure of the thunderstorm. However, space-based platforms in LEO are only in view of a given thunderstorm for a few minutes, and there might not be enough data during the overpass to generate robust statistics. This will be particularly problematic for those low flash rate oceanic storms that space-based platforms are uniquely capable of observing. Another issue is that the level of detail provided by space-based measurements is considerably less than what would be seen by a typical LMA. Even in this case, where we have dozens of sources (which is rare), only three sources occur in the initial breakdown period (one of which is ambiguous). There is not enough data to confidently resolve the upward propagation of the negative leader in most FORTE flashes.

Despite this lack of data from individual flashes, we can still examine the statistical behavior of the initial negative leader breakdown, as well as other portions of the flash, by aggregating the source altitude distributions from multiple flashes. In Figure 10, we compute the VHF cumulative altitude distributions for each point over the duration of LLS flashes over land (top row), the coastal ocean (middle row), and the open ocean (bottom row). The left column uses linear temporal bins to detail the initial 60 ms of the flash, while the center column accumulates data in logarithmic bins out to 1 s after the flash start. Note that the reference time for the start of the flash in the

23335084, 2022, 9, Downloaded from https://agupubs.onlinelibrary.wiley.com/doi/10.1029/2022EA002404 by Los Alamos National Laboratory, Wiley Online Library on [11/10/2022]. See the Terms and Conditions (https://onlinelibrary.wiley.com/terms-and-conditions) on Wiley Online Library for rules of use; OA articles are governed by the applicable Creative Commons License

10.1029/2022EA002404

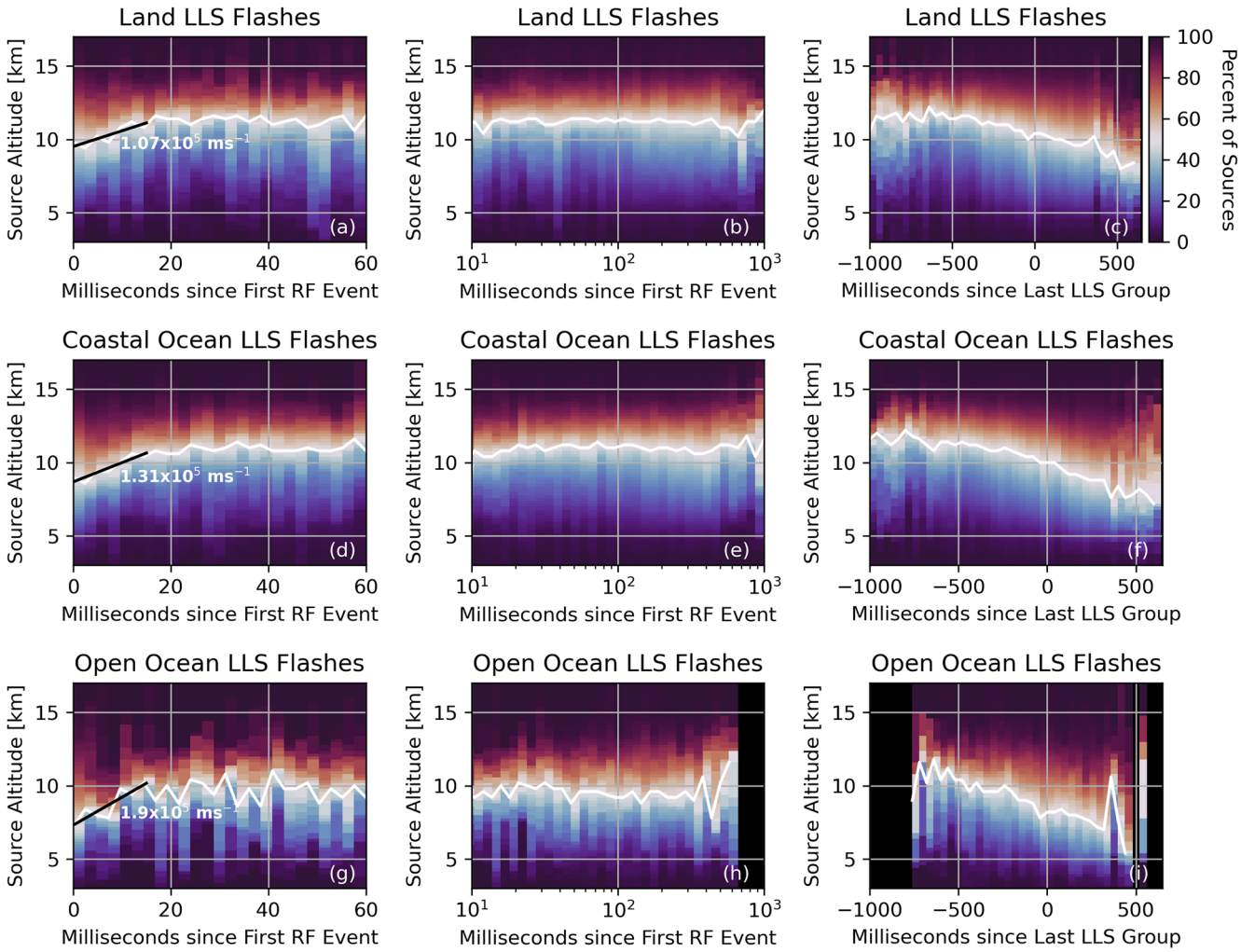

Figure 10. Cumulative distributions of source attitude at each point over the duration of land (top row), coastal ocean (middle row) and open (bottom) flashes. Early activity in the flash is shown in the left column with linear fits to the median altitude curve over the first 15 ms of flash activity overlaid. The slopes of these lines approximate vertical propagation speeds for negative leaders. Altitude profiles at all points over the flash duration are shown in the central column relative to the flash start. The right column shows flash altitude variations surrounding the final lightning location system group in the flash.

left two columns is defined as the time of its first RF source, not the start of optical emissions detected by the LLS. Finally, the right column details variations in source altitude around the final group from the flash detected by the LLS. Median values are also indicated with solid white lines in each panel.

The initial breakdown phase is evident as a shift in the source altitude profiles toward higher altitudes over the first ~20 ms of the flash in land-based (Figure 10a), coastal ocean (Figure 10d), and open ocean (Figure 10g) flashes. However, the rate at which the altitudes increase differs between regions, implying that negative leaders propagate upwards at different speeds. If we fit the median altitude in the first 15 ms of the flash to a linear model (black line), we get typical leader propagation speeds of 1.07×10^5 ms^{-1} over land, 1.31×10^5 ms^{-1} over the coastal ocean, and 1.90×10^5 ms^{-1} over the open ocean. These are all within the range reported by Shao and Krehbiel (1996). The apparent difference in propagation speed between land and ocean regions seems to be linked to variations in flash initiation altitude. Previous studies have noted cases of particularly fast negative leaders in oceanic return strokes (e.g., Wu et al., 2021). These variations in propagation speed may be physical, but additional data are needed to verify whether they are robust.

After the initial breakdown period, the distributions become flat, with little change in the source altitude profile over time in the flash (Figures 10b, 10e, and 10h). Despite this, we have identified cases of later flash activity occurring at lower altitudes—either as abrupt shifts in the source altitude profile after the upper charge layer

23335084, 2022, 9, Downloaded from https://agupubs.onlinelibrary.wiley.com/doi/10.1029/2022EA002404 by Los Alamos National Laboratory, Wiley Online Library on [11/10/2022]. See the Terms and Conditions (https://onlinelibrary.wiley.com/terms-and-conditions) on Wiley Online Library for rules of use; OA articles are governed by the applicable Creative Commons License

23335084, 2022, 9, Downloaded from https://agupubs.onlinelibrary.wiley.com/doi/10.1029/2022EA002404 by Los Alamos National Laboratory, Wiley Online Library on [11/10/2022]. See the Terms and Conditions (https://onlinelibrary.wiley.com/terms-and-conditions) on Wiley Online Library for rules of use; OA articles are governed by the applicable Creative Commons License

becomes cut off, as in Peterson et al. (2021b), or as gradual shifts from leaders descending over time, as in the case from Figure 9. Altitude profiles shifting toward lower altitude sources would be problematic for optical detection, as the increased optical depth of cloud above the sources would make their emissions harder to detect by the LLS.

Because Figures 10b, 10e, and 10h compute source altitude profiles relative to the flash start and flashes have variable durations, these distributions mask the behavior at the end of the flash. To highlight activity late in the flash, particularly as it relates to optical detection, Figures 10c, 10f, and 10i compute source altitude profiles relative to the final LLS group detected from the flash. In these final distributions in Figure 10, a clear downward drift can be noted at the end of the LLS flash. The median source altitude coincident with the final group (0 ms) or VHF sources that were detected after the LLS stopped triggering (>0 ms) is close to or below 10 km in land (Figure 10c) and coastal ocean (Figure 10f) regions, and 8 km in open ocean regions (Figure 10i).

A 10 km altitude is significant because it is the approximate altitude where optical coincidence was previously reported to fall off (Light & Jacobson, 2002). Source altitudes falling below this altitude at the end of the LLS flash supports the idea that LIS and LLS flashes terminate not because they cease emitting, but because the activity can no longer be detected by a lightning imager. Other optical sensors like the FORTE PDD are capable of resolving optical emission after the final group (Peterson, 2022a). This would explain why the final group in LIS flashes often is particularly radiant (Peterson & Rudlosky, 2019). When leader activity is confined to low altitudes, the faint emissions from the developing leader are attenuated beyond the detection limits of the instrument, but radiant pulses from strokes and K-changes are still recorded. We saw this previously in Peterson et al. (2021b) where the only emissions detected from the hybrid CG flash after the upper layer became cut off were intense optical pulses from K-changes. The frequent faint emissions from the developing leader that dominated the early part of the flash were not resolved in this later period.

In our final flash level analysis, we compute the initiation and propagation altitudes for FORTE flashes. To mitigate errors from spurious sources, we define the initiation altitude as the lowest altitude of all sources during the initial breakdown phase within 15 ms of the flash start. Then, the propagation altitude is defined as the average altitude of all sources in the LLS flash. For this analysis, we will allow the ambiguous sources (black dots in 9b) to better resolve activity in negative charge layers. Profiles of initiation altitude (left column) and propagation altitude (right column) are shown in Figure 11 for flashes over land (top row), the coastal ocean (middle row), and the open ocean (bottom row).

The initiation altitude profile for land-based flashes has two peaks: a lower peak at 7 km altitude and an upper peak at 10–11 km altitude. Oceanic flashes are more likely to have their initial sources at low altitudes. The lower peak (6 km altitude) is dominant over the upper peak for the coastal ocean (Figure 11c), while the upper peak is hardly apparent for flashes over the open ocean (Figure 11e), where the lower peak occurs at 4 km altitude. The peaks in the propagation altitude distribution, meanwhile, are similar between land and the coastal ocean, though the oceanic flashes are still more likely to propagate at lower altitudes, overall. The propagation altitude profile for flashes over the open ocean is single-peaked with a maximum of 7 km altitude.

These altitude profiles do not consider variations in flash initiation or propagation altitudes by flash type (IC or CG) or storm type (as in Mecikalski and Carey, 2018), which vary by region across the Earth. Flash type and storm type partitioning are topics that we plan to consider in future work.

4. Conclusion

We leverage coincident detections of lightning events by the FORTE RF system and LLS to document the altitude distributions of in-cloud lightning sources across the globe. Previous FORTE studies generated profiles of VHF source altitudes (Light & Jacobson, 2002) but were limited by a small sample size. Using the full FORTE RF record and improved pulse extraction methods, and by relaxing the criteria for LLS coincidence, we are able to characterize the vertical distributions of VHF sources over large swaths of the Earth.

The negative leaders that are prevalent emitters of VHF radiation most often propagate through the upper positive charge layer of ordinary thunderstorms. For this reason, the FORTE VHF source altitude distributions generally peak at 11 km altitude. However, VHF sources at lower altitudes, including initial breakdowns and later activity in lower negative charge layers, can also be detected from space. We find that typical vertical development speeds

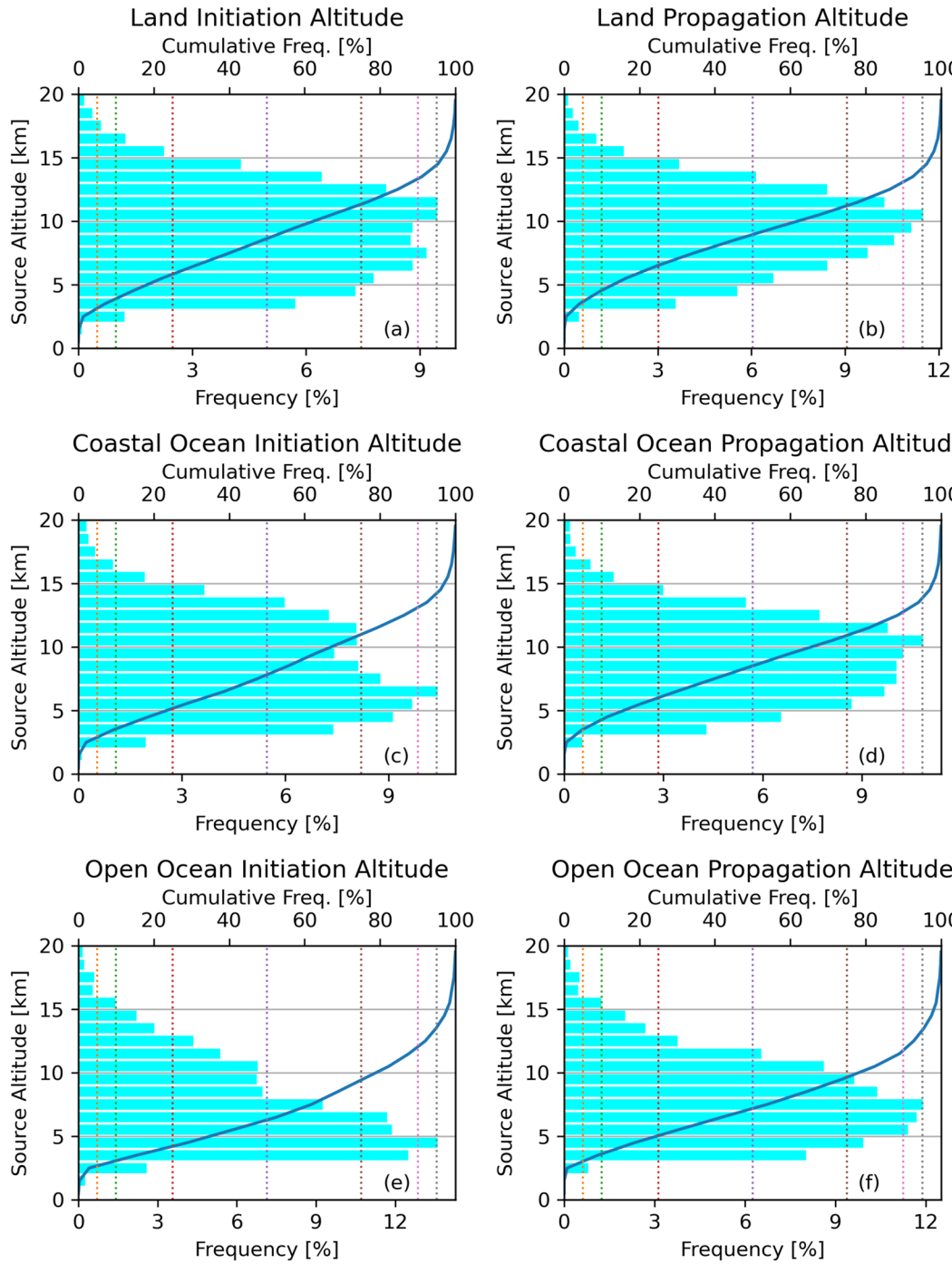

Figure 11. Profiles of flash initiation altitude (left column) and propagation altitude (right column) for flashes over land (top row), the coastal ocean (middle row), and the open ocean (bottom row).

of negative leaders appear to differ between land (1.07×10^5 ms^{-1}), coastal oceanic regions (1.31×10^5 ms^{-1}), and the open ocean (1.90×10^5 ms^{-1}). However, while FORTE can resolve the lightning phenomena required for automated charge layer identification—for example, with the chargepol algorithm (Medina et al., 2021)—the level of unambiguous detail we can resolve is usually not sufficient to characterize the upward developing leader on a per-flash basis, while the limited view time provided by the low FORTE orbit inhibits robust statistics from individual thunderstorms.

23335084, 2022, 9, Downloaded from https://agupubs.onlinelibrary.wiley.com/doi/10.1029/2022EA002404 by Los Alamos National Laboratory, Wiley Online Library on [11/10/2022]. See the Terms and Conditions (https://onlinelibrary.wiley.com/terms-and-conditions) on Wiley Online Library for rules of use; OA articles are governed by the applicable Creative Commons License

23335084, 2022, 9, Downloaded from https://agupubs.onlinelibrary.wiley.com/doi/10.1029/2022EA002404 by Los Alamos National Laboratory, Wiley Online Library on [11/10/2022]. See the Terms and Conditions (https://onlinelibrary.wiley.com/terms-and-conditions) on Wiley Online Library for rules of use; OA articles are governed by the applicable Creative Commons License

Low-altitude sources are found to be particularly common in winter and/or oceanic regions outside of the tropics, as well as over the La Plata basin, where large MCSs produce abundant stratiform lightning, including megaflashes. We previously showed that an individual large stratiform flash can produce hundreds of FORTE RF events with impulsive VHF sources clustered in a layer between 4 and 8 km altitude (Peterson et al., 2021a). Regions with frequent stratiform lightning are thus expected to have source altitude profiles with significant contributions from both high-altitude convective sources and low-altitude stratiform sources. Tropical regions, meanwhile, had the tallest source altitude profiles, with the Colombia and Panama regions having the greatest 75th percentile source altitude (13.6 km) of the regions considered.

Regional factors, including seasonal variations in storm type, are shown to have a pronounced impact on the VHF source altitude profiles, as well as on the flash initiation and propagation heights. We provide a high-level overview of some of the variations in this new data set, but further in-depth analysis is required to explain all of the trends therein. In future work, we plan to create distinct altitude profiles for CG and IC flashes, as well as various storm types (as in Mecikalski and Carey, 2018). It is expected that these global measurements will be valuable for global climate modeling, particularly for LNOx models, that currently derive lightning altitudes from parameterizations based on environmental variables. Further applications of this data will also be explored in future work.

Data Availability Statement

Version 2 of the FORTE lightning altitude data used in this study are available at the Harvard Dataverse via https://doi.org/10.7910/DVN/0ZWPTL (Peterson, 2022b).

Acknowledgments
Los Alamos National Laboratory is operated by Triad National Security, LLC, under contract number 89233218CNA000001. As we celebrate the 25th anniversary of the fast on-orbit recording of transient events (FORTE's) launch, we would like to extend a special thank you to the FORTE science team at LANL and SNL for all of their efforts over the past three decades in making the FORTE program a success.

References

Albrecht, R. I., Goodman, S. J., Buechler, D. E., Blakeslee, R. J., & Christian, H. J. (2016). Where are the lightning hotspots on Earth? *Bulletin of the American Meteorological Society*, *97*(11), 2051–2068. https://doi.org/10.1175/bams-d-14-00193.1

Bitzer, P. M. (2017). Global distribution and properties of continuing current in lightning. *Journal of Geophysical Research: Atmospheres*, *122*(2), 1033–1041. https://doi.org/10.1002/2016jd025532

Carey, L. D., Koshak, W., Peterson, H., & Mecikalski, R. M. (2016). The kinematic and microphysical control of lightning rate, extent, and NOX production. *Journal of Geophysical Research: Atmospheres*, *121*(13), 7975–7989. https://doi.org/10.1002/2015jd024703

Cecil, D. J., Buechler, D. E., & Blakeslee, R. J. (2014). Gridded lightning climatology from TRMM-LIS and OTD: Dataset description. *Atmospheric Research*, *135*, 404–414. https://doi.org/10.1016/j.atmosres.2012.06.028

Chameides, W., & Walker, J. C. (1973). A photochemical theory of tropospheric ozone. *Journal of Geophysical Research*, *78*(36), 8751–8760. https://doi.org/10.1029/jc078i036p08751

Crutzen, P. (1973). A discussion of the chemistry of some minor constituents in the stratosphere and troposphere. *Pure and Applied Geophysics*, *106*(1), 1385–1399. https://doi.org/10.1007/bf00881092

Crutzen, P. J., Heidt, L. E., Krasnec, J. P., Pollock, W. H., & Seiler, W. (1979). Biomass burning as a source of atmospheric gases CO, H_2, N_2O, NO, CH_3Cl and COS. *Nature*, *282*(5736), 253–256. https://doi.org/10.1038/282253a0

Cummins, K. L., Murphy, M. J., Bardo, E. A., Hiscox, W. L., Pyle, R. B., & Pifer, A. E. (1998). A combined TOA/MDF technology upgrade of the US national lightning detection network. *Journal of Geophysical Research*, *103*(D8), 9035–9044. https://doi.org/10.1029/98jd00153

DeCaria, A. J., Pickering, K. E., Stenchikov, G. L., Scala, J. R., Stith, J. L., Dye, J. E., et al. (2000). A cloud-scale model study of lightning-generated NOx in an individual thunderstorm during STERAO-A. *Journal of Geophysical Research*, *105*(D9), 11601–11616. https://doi.org/10.1029/2000jd900033

Ely, B. L., Orville, R. E., Carey, L. D., & Hodapp, C. L. (2008). Evolution of the total lightning structure in a leading-line, trailing-stratiform mesoscale convective system over Houston, Texas. *Journal of Geophysical Research*, *113*(D8), D08114. https://doi.org/10.1029/2007jd008445

Fierro, A. O., Shao, X. M., Hamlin, T., Reisner, J. M., & Harlin, J. (2011). Evolution of eyewall convective events as indicated by intracloud and cloud-to-ground lightning activity during the rapid intensification of hurricanes Rita and Katrina. *Monthly Weather Review*, *139*(5), 1492–1504. https://doi.org/10.1175/2010mwr3532.1

Fishman, J., Solomon, S., & Crutzen, P. J. (1979). Observational and theoretical evidence in support of a significant in-situ photochemical source of tropospheric ozone. *Tellus*, *31*(5), 432–446. https://doi.org/10.1111/j.2153-3490.1979.tb00922.x

Goodman, S. J., Mach, D., Koshak, W. J., & Blakeslee, R. J. (2012). GLM lightning cluster filter algorithm (LCFA) algorithm theoretical basis document (ATBD). NOAA NESDIS center for satellite applications and research. Retrieved from https://www.star.nesdis.noaa.gov/goesr/docs/ATBD/LCFA.pdf

H. J., Christian, R. J., Blakeslee, S. J., Goodman, & D. M., Mach, (Eds.). (2000). Algorithm theoretical basis document (ATBD) for the lightning imaging sensor (LIS), NASA/Marshall space flight center. Retrieved from http://eospso.gsfc.nasa.gov/atbd/listables.html

Ivanov, M. F., Kiverin, A. D., Klumov, B. A., & Fortov, V. E. (2014). From combustion and detonation to nitrogen oxides. *Physics-Uspekhi*, *57*(3), 234–249. https://doi.org/10.3367/ufne.0184.201403c.0247

Jacobson, A. R., Knox, S. O., Franz, R., & Enemark, D. C. (1999). FORTE observations of lightning radio-frequency signatures: Capabilities and basic results. *Radio Science*, *34*(2), 337–354. https://doi.org/10.1029/1998rs900043

Jayaratne, E. R., Saunders, C. P. R., & Hallett, J. (1983). Laboratory studies of the charging of soft-hail during ice crystal interactions. *Quarterly Journal of the Royal Meteorological Society*, *109*(461), 609–630. https://doi.org/10.1002/qj.49710946111

Kirkland, M. W., Suszcynsky, D. M., Guillen, J. L. L., & Green, J. L. (2001). Optical observations of terrestrial lightning by the FORTE satellite photodiode detector. *Journal of Geophysical Research*, *106*(D24), 33499–33509. https://doi.org/10.1029/2000jd000190

Labrador, L. J., Von Kuhlmann, R., & Lawrence, M. G. (2005). The effects of lightning-produced NOx and its vertical distribution on atmospheric chemistry: Sensitivity simulations with MATCH-MPIC. *Atmospheric Chemistry and Physics*, *5*(7), 1815–1834. https://doi.org/10.5194/acp-5-1815-2005

Lacis, A. A., Wuebbles, D. J., & Logan, J. A. (1990). Radiative forcing of climate by changes in the vertical distribution of ozone. *Journal of Geophysical Research*, *95*(D7), 9971–9981. https://doi.org/10.1029/jd095id07p09971

Lang, T. J., Pédeboy, S., Rison, W., Cerveny, R. S., Montanyà, J., Chauzy, S., et al. (2017). WMO world record lightning extremes: Longest reported flash distance and longest reported flash duration. *Bulletin of the American Meteorological Society*, *98*(6), 1153–1168. https://doi.org/10.1175/bams-d-16-0061.1

Lang, T. J., & Rutledge, S. A. (2008). Kinematic, microphysical, and electrical aspects of an asymmetric bow-echo mesoscale convective system observed during STEPS 2000. *Journal of Geophysical Research*, *113*(D8), D08213. https://doi.org/10.1029/2006jd007709

Lang, T. J., Rutledge, S. A., & Wiens, K. C. (2004). Origins of positive cloud-to-ground lightning flashes in the stratiform region of a mesoscale convective system. *Geophysical Research Letters*, *31*(10). https://doi.org/10.1029/2004gl019823

Light, T. E., Suszcynsky, D. M., & Jacobson, A. R. (2001). Coincident radio frequency and optical emissions from lightning, observed with the FORTE satellite. *Journal of Geophysical Research*, *106*(D22), 28223–28231. https://doi.org/10.1029/2001JD000727

Light, T. E. L. (2020). A retrospective of findings from the FORTE satellite mission. *Journal of Geophysical Research: Atmospheres*, *125*(9), e2019JD032264.

Light, T. E. L., & Jacobson, A. R. (2002). Characteristics of impulsive VHF lightning signals observed by the FORTE satellite. *Journal of Geophysical Research*, *107*(D24), ACL-8-1–ACL-8-8. https://doi.org/10.1029/2001jd001585

López, J. A., Montanyà, J., van der Velde, O. A., Pineda, N., Salvador, A., Romero, D., et al. (2019). Charge structure of two tropical thunderstorms in Colombia. *Journal of Geophysical Research: Atmospheres*, *124*(10), 5503–5515. https://doi.org/10.1029/2018jd029188

Luo, C., Wang, Y., & Koshak, W. J. (2017). Development of a self-consistent lightning NOx simulation in large-scale 3-D models. *Journal of Geophysical Research: Atmospheres*, *122*(5), 3141–3154. https://doi.org/10.1002/2016jd026225

Lyons, W. A., Bruning, E. C., Warner, T. A., MacGorman, D. R., Edgington, S., Tillier, C., & Mlynarczyk, J. (2020). Megaflashes: Just how long can a lightning discharge get? *Bulletin of the American Meteorological Society*, *101*(1), E73–E86. https://doi.org/10.1175/bams-d-19-0033.a

Mach, D. M., Christian, H. J., Blakeslee, R. J., Boccippio, D. J., Goodman, S. J., & Boeck, W. L. (2007). Performance assessment of the optical transient detector and lightning imaging sensor. *Journal of Geophysical Research*, *112*(D9), D09210. https://doi.org/10.1029/2006jd007787

Mansell, E. R., MacGorman, D. R., Ziegler, C. L., & Straka, J. M. (2005). Charge structure and lightning sensitivity in a simulated multicell thunderstorm. *Journal of Geophysical Research*, *110*(D12), D12101. https://doi.org/10.1029/2004jd005287

Marshall, T. C., & Rust, W. D. (1991). Electric field soundings through thunderstorms. *Journal of Geophysical Research*, *96*(D12), 22297–22306. https://doi.org/10.1029/91jd02486

Marshall, T. C., Rust, W. D., Winn, W. P., & Gilbert, K. E. (1989). Electrical structure in two thunderstorm anvil clouds. *Journal of Geophysical Research*, *94*(D2), 2171–2181. https://doi.org/10.1029/jd094id02p02171

Mecikalski, R. M., & Carey, L. D. (2018). Radar reflectivity and altitude distributions of lightning as a function of IC, CG, and HY flashes: Implications for LNOx production. *Journal of Geophysical Research: Atmospheres*, *123*(22), 12–796. https://doi.org/10.1029/2018jd029263

Medina, B. L., Carey, L. D., Lang, T. J., Bitzer, P. M., Deierling, W., & Zhu, Y. (2021). Characterizing charge structure in Central Argentina thunderstorms during RELAMPAGO utilizing a new charge layer polarity identification method. *Earth and Space Science*, *8*(8), e2021EA001803. https://doi.org/10.1029/2021ea001803

Peterson, M. (2019). Research applications for the geostationary lightning mapper operational lightning flash data product. *Journal of Geophysical Research: Atmospheres*, *124*(17–18), 10205–10231. https://doi.org/10.1029/2019jd031054

Peterson, M. (2021). Where are the most extraordinary lightning megaflashes in the Americas? *Bulletin of the American Meteorological Society*, *102*(3), E660–E671. https://doi.org/10.1175/bams-d-20-0178.1

Peterson, M. (2022a). Combined optical and radio-frequency perspectives on the time evolution of lightning measured by the FORTE satellite. *Earth and Space Science*, *9*(6), e2022EA002281. https://doi.org/10.1029/2022ea002281

Peterson, M. (2022b). FORTE lightning altitude data. Harvard Dataverse, V2 [dataset] https://doi.org/10.7910/DVN/0ZWPTL .

Peterson, M. (2022c). FORTE measurements of global optical lightning waveforms and implications for optical lightning detection. *Earth and Space Science*, *9*(6), e2022EA002280. https://doi.org/10.1029/2022ea002280

Peterson, M., Deierling, W., Liu, C., Mach, D., & Kalb, C. (2017). The properties of optical lightning flashes and the clouds they illuminate. *Journal of Geophysical Research: Atmospheres*, *122*(1), 423–442. https://doi.org/10.1002/2016jd025312

Peterson, M., Light, T. E., & Shao, X. M. (2021a). Combined optical and radio-frequency measurements of a lightning megaflash by the FORTE satellite. *Journal of Geophysical Research: Atmospheres*, *126*(15), e2020JD034411. https://doi.org/10.1029/2020jd034411

Peterson, M., Light, T. E. L., & Shao, X.-M. (2021b). Combined optical and radio-frequency perspectives on a hybrid cloud-to-ground lightning flash observed by the FORTE satellite. *Journal of Geophysical Research: Atmospheres*, *126*(7), e2020JD034152. https://doi.org/10.1029/2020JD034152

Peterson, M., Mach, D., & Buechler, D. (2021c). A global LIS/OTD climatology of lightning flash extent density. *Journal of Geophysical Research: Atmospheres*, *126*(8), e2020JD033885. https://doi.org/10.1029/2020jd033885

Peterson, M., & Rudlosky, S. (2019). The time evolution of optical lightning flashes. *Journal of Geophysical Research: Atmospheres*, *124*(1), 333–349. https://doi.org/10.1029/2018jd028741

Peterson, M., Rudlosky, S., & Deierling, W. (2017). The evolution and structure of extreme optical lightning flashes. *Journal of Geophysical Research: Atmospheres*, *122*(24), 13–370. https://doi.org/10.1002/2017jd026855

Peterson, M., & Stano, G. (2021). The hazards posed by mesoscale lightning megaflashes. *Earth Interactions*, *25*(1), 46–56. https://doi.org/10.1175/ei-d-20-0016.1

Pickering, K. E., Wang, Y., Tao, W. K., Price, C., & Müller, J. F. (1998). Vertical distributions of lightning NOx for use in regional and global chemical transport models. *Journal of Geophysical Research*, *103*(D23), 31203–31216. https://doi.org/10.1029/98jd02651

Rakov, V. A., & Uman, M. A. (2003). *Lightning: Physics and effects*. Cambridge University Press.

Reynolds, S. E., Brook, M., & Gourley, M. F. (1957). Thunderstorm charge separation. *Journal of Meteorology*, *14*(5), 163–178. https://doi.org/10.1175/1520-0469(1957)014<0426:tcs>2.0.co;2

Rison, W., Thomas, R. J., Krehbiel, P. R., Hamlin, T., & Harlin, J. (1999). A GPS-based three-dimensional lightning mapping system: Initial observations in central New Mexico. *Geophysical Research Letters*, *26*(23), 3573–3576. https://doi.org/10.1029/1999gl010856

Saunders, C. P. R., Keith, W. D., & Mitzeva, R. P. (1991). The effect of liquid water on thunderstorm charging. *Journal of Geophysical Research*, *96*(D6), 11007–11017. https://doi.org/10.1029/91jd00970

Saunders, C. P. R., & Peck, S. L. (1998). Laboratory studies of the influence of the rime accretion rate on charge transfer during crystal/graupel collisions. *Journal of Geophysical Research*, *103*(D12), 13949–13956. https://doi.org/10.1029/97jd02644

23335084, 2022, 9, Downloaded from https://agupubs.onlinelibrary.wiley.com/doi/10.1029/2022EA002404 by Los Alamos National Laboratory, Wiley Online Library on [11/10/2022]. See the Terms and Conditions (https://onlinelibrary.wiley.com/terms-and-conditions) on Wiley Online Library for rules of use; OA articles are governed by the applicable Creative Commons License

Schuur, T. J., & Rutledge, S. A. (2000). Electrification of stratiform regions in mesoscale convective systems. Part I: An observational comparison of symmetric and asymmetric MCSs. *Journal of the Atmospheric Sciences*, *57*(13), 1961–1982. https://doi.org/10.1175/1520-0469(2000)057<1961:eosrim>2.0.co;2

Seiler, W., & Crutzen, P. J. (1980). Estimates of gross and net fluxes of carbon between the biosphere and the atmosphere from biomass burning. *Climatic Change*, *2*(3), 207–247. https://doi.org/10.1007/bf00137988

Shao, X.-M., & Jacobson, A. R. (2001). Polarization observations of broadband VHF signals by the FORTE satellite. *Radio Science*, *36*(6), 1573–1589. https://doi.org/10.1029/2000RS002600

Shao, X. M., & Krehbiel, P. R. (1996). The spatial and temporal development of intracloud lightning. *Journal of Geophysical Research*, *101*(D21), 26641–26668. https://doi.org/10.1029/96jd01803

Simpson, G. C., & Scrase, F. J. (1937). The distribution of electricity in thunderclouds. *Proceedings of the Royal Society of London. Series A-Mathematical and Physical Sciences*, *161*(906), 309–352.

Stolzenburg, M., Rust, W. D., Smull, B. F., & Marshall, T. C. (1998). Electrical structure in thunderstorm convective regions: 1. Mesoscale convective systems. *Journal of Geophysical Research*, *103*(D12), 14059–14078. https://doi.org/10.1029/97jd03546

Suszcynsky, D. M., & Heavner, M. J. (2003). Narrow bipolar events as indicators of thunderstorm convective strength. *Geophysical Research Letters*, *30*(17). https://doi.org/10.1029/2003gl017834

Suszcynsky, D. M., Kirkland, M. W., Jacobson, A. R., Franz, R. C., Knox, S. O., Guillen, J. L. L., & Green, J. L. (2000). FORTE observations of simultaneous VHF and optical emissions from lightning: Basic phenomenology. *Journal of Geophysical Research*, *105*(D2), 2191–2201. https://doi.org/10.1029/1999jd900993

Suszcynsky, D. M., Light, T. E., Davis, S., Green, J. L., Guillen, J. L. L., & Myre, W. (2001). Coordinated observations of optical lightning from space using the FORTE photodiode detector and CCD imager. *Journal of Geophysical Research*, *106*(D16), 17897–17906. https://doi.org/10.1029/2001jd900199

Takahashi, T. (1978). Riming electrification as a charge generation mechanism in thunderstorms. *Journal of the Atmospheric Sciences*, *35*(8), 1536–1548. https://doi.org/10.1175/1520-0469(1978)035<1536:reaacg>2.0.co;2

Takahashi, T., & Miyawaki, K. (2002). Reexamination of riming electrification in a wind tunnel. *Journal of the Atmospheric Sciences*, *59*(5), 1018–1025. https://doi.org/10.1175/1520-0469(2002)059<1018:roreia>2.0.co;2

Thomas, R. J., Krehbiel, P. R., Rison, W., Hunyady, S. J., Winn, W. P., Hamlin, T., & Harlin, J. (2004). Accuracy of the lightning mapping array. *Journal of Geophysical Research*, *109*(D14), D14207. https://doi.org/10.1029/2004jd004549

Tie, X., Zhang, R., Brasseur, G., & Lei, W. (2002). Global NOx production by lightning. *Journal of Atmospheric Chemistry*, *43*(1), 61–74. https://doi.org/10.1023/a:1016145719608

Williams, E. (2018). Lightning activity in winter storms: A meteorological and cloud microphysical perspective. *IEEJ Transactions on Power and Energy*, *138*(5), 364–373. https://doi.org/10.1541/ieejpes.138.364

Williams, E. R. (1989). The tripole structure of thunderstorms. *Journal of Geophysical Research*, *94*(D11), 13151–13167. https://doi.org/10.1029/jd094id11p13151

Williams, E. R., & Sátori, G. (2004). Lightning, thermodynamic and hydrological comparison of the two tropical continental chimneys. *Journal of Atmospheric and Solar-Terrestrial Physics*, *66*(13–14), 1213–1231. https://doi.org/10.1016/j.jastp.2004.05.015

Wilson, C. T. R. (1920). III. Investigations on lightning discharges and on the electric field of thunderstorms. *Philosophical Transactions of the Royal Society of London - Series A: Containing Papers of a Mathematical or Physical Character*, *221*(582–593), 73–115.

Wu, T., Wang, D., Huang, H., & Takagi, N. (2021). The strongest negative lightning strokes in winter thunderstorms in Japan. *Geophysical Research Letters*, *48*(21), e2021GL095525. https://doi.org/10.1029/2021gl095525

Yamamoto, M. K., Higuchi, A., & Nakamura, K. (2006). Vertical and horizontal structure of winter precipitation systems over the western Pacific around Japan using TRMM data. *Journal of Geophysical Research*, *111*(D13), D13108. https://doi.org/10.1029/2005jd006412

23335084, 2022, 9, Downloaded from https://agupubs.onlinelibrary.wiley.com/doi/10.1029/2022EA002404 by Los Alamos National Laboratory, Wiley Online Library on [11/10/2022]. See the Terms and Conditions (https://onlinelibrary.wiley.com/terms-and-conditions) on Wiley Online Library for rules of use; OA articles are governed by the applicable Creative Commons License